
BLINDSIGHT: HARNESSING SPARSITY FOR EFFICIENT VISION-LANGUAGE MODELS

Tharun Adithya Srikrishnan*, Deval Shah*, Timothy Hein[†], Ahmed Hassan, Stephen Youn[‡], Steven K. Reinhardt
Advanced Micro Devices, Inc. (AMD)

ABSTRACT

Large vision-language models (VLMs) enable joint processing of text and images. However, incorporating vision data significantly increases the prompt length, resulting in a longer time to first token (TTFT). This bottleneck can be alleviated by leveraging the inherent sparsity in the attention computation. Analyzing these attention patterns in VLMs when processing a series of images, we observe the absence of inter-image attention in a substantial portion of layers. Based on this, we propose **BlindSight**: an approach to optimize multi-image VLM inference using an input-template-aware attention sparsity mask with no runtime overhead. We utilize a dataset to derive a prompt-agnostic categorization for attention heads: Dense, Sink, Intra-Image, and Intra-Image+Sink. We develop a Triton-based GPU kernel to leverage this sparsity. BlindSight achieves a 1.8-3.2 \times speedup in the attention computation (prompt length 36K-300K). BlindSight generalizes across VLMs (Qwen2-VL, Qwen2.5-VL, Gemma 3), with only a 0.78% absolute accuracy degradation on average on multi-image comprehension benchmarks. Finally, we advocate for the design of efficient VLMs that combine BlindSight-inspired sparse and dense layers.

1 INTRODUCTION

Vision-language models (VLMs) have shown impressive capabilities in processing visual and textual information together Wang et al. (2024b); Bai et al. (2025b); Meta AI (2025); Gemma team (2025); Chen et al. (2024b). This has opened up several avenues for application in fields such as autonomous driving Hu et al. (2023); Tian et al. (2024), finance Wang et al. (2023); Bhatia et al. (2024), medical research Delbrouck et al. (2022); Hartsock & Rasool (2024) and robotics Black et al. (2024); Brohan et al. (2023). VLMs often incorporate pre-trained vision encoders, with a transformer-based multimodal processing module to process both language and vision tokens. The context length in VLM queries is often significantly higher than in text-only models due to the large number of tokens introduced by images and videos. Applications utilizing videos or high-resolution images would further increase the context length.

Attention dominates during inference for longer context lengths due to its quadratic computational complexity. The time to first token (TTFT) (i.e., prefill time) for long prompts can be in the order of minutes and may even require distributed computation Liu et al. (2024); Brandon et al. (2023). In Qwen2.5-VL (32B) Bai et al. (2025b), the attention operation accounts for 53% of the total prefill time when processing an input of 8K tokens. The real-time application of VLMs is therefore limited by the increase in TTFT. Another consequence of longer context lengths is a substantial expansion of the KV cache during decoding, which in turn increases system memory requirements. This impact is expected to worsen with test-time scaling Snell et al. (2024); Yao et al. (2023); Muennighoff et al. (2025); Sadhukhan et al. (2025).

VLMs differ from LLMs in that their inputs typically consist of an interleaved sequence of images and text. The length of each image segment may vary depending on the image resolution and tokenization approach. Previous works have observed that attention matrices tend to be sparse Zaheer

*Equal contribution

[†] Internship at AMD

[‡] Work performed while at AMD

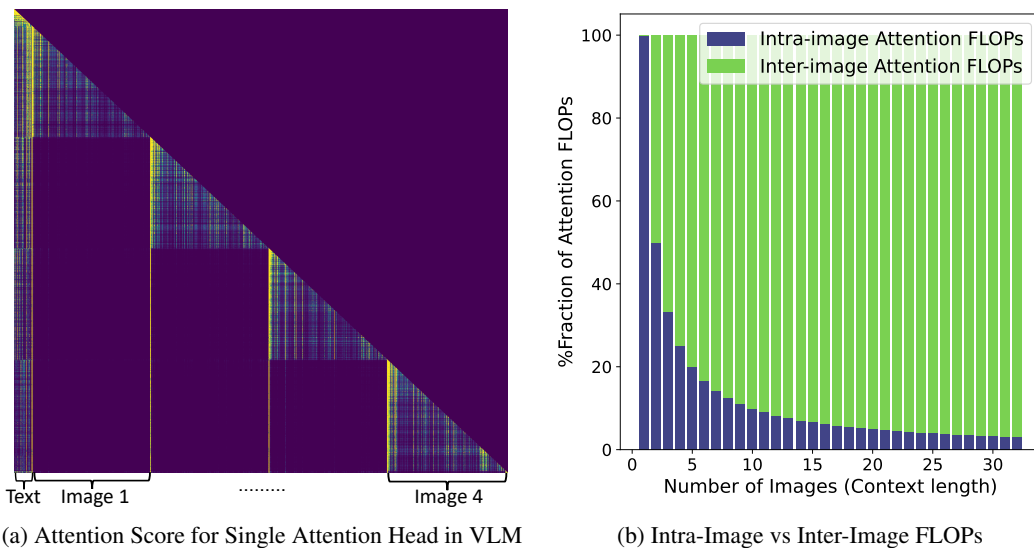


Figure 1: (a) Attention matrix for an attention head in Qwen2.5-VL (7B). The input prompt consists of text followed by 4 images. Notice that the image tokens vastly outnumber text tokens. (b) Impact of number of input images on intra/inter-image attention FLOPs.

et al. (2021); Beltagy et al. (2020). We also observe this phenomenon in VLMs, as shown in Fig. 1a. This sparsity can be exploited to accelerate the prefill time by masking out computations corresponding to the sparse elements. Existing VLM-specific sparsity-based optimization techniques, such as MMInference Li et al. (2025) and Look-M Wan et al. (2024) rely on computing partial attention score-based metrics during inference to identify intra-modality sparsification opportunities, at the cost of additional memory and latency. An offline sparsity characterization approach such as ours can remove such overheads from the inference path.

We observe that inter-image attention dominates the overall attention computation as the number of images in the prompt increases (Fig. 1b). Based on this observation, we specifically focus on the *inter-image sparsity patterns in VLMs that can be derived without additional runtime computation*. We characterize the attention matrix for several multi-image VLMs such as Qwen2-VL Wang et al. (2024b), Qwen2.5-VL Bai et al. (2025b) and Gemma 3 Gemma team (2025).

We categorize sparsity patterns to derive distinct groups defined by the input prompt template (i.e., from the position of the text and images). We match attention heads to four templates in Section 3.2: a *Dense* pattern and three sparse patterns (*Sink*, *Intra-Image*, and *Intra-Image+Sink*). We consistently observe these sparsity patterns across model architectures, image resolution and tokenization strategies (including token compression); demonstrating that the proposed patterns generalize across a wide range of models and evaluations. We also observe an input-dependent variation in the optimal sparsity template selected per head. We determine that an aggregation scheme can convert the prompt-dependent mask-template choice into a prompt-independent one (Section 4). **BlindSight** consists of two steps:

- **Prompt-level Characterization:** Metric-based approach to select the sparsity type for a given attention head with minimum accuracy impact.
- **Dataset-level Aggregation:** Rule-based approach to aggregate prompt-level attention head categorizations across a characterization dataset.

To our knowledge, BlindSight is the first technique that uncovers and leverages the image-sink based sparsity that emerges in VLMs processing multi-image prompts. We note the specific difference between multi-image and video processing in recent VLMs due to delimiter tokens (Section 7). Our contributions can be summarized as follows:

- Characterized attention patterns for several VLMs and identified four attention head categories: *Dense*, *Sink*, *Intra-Image*, and *Intra-Image+Sink*.

- Developed **BlindSight**, an approach to select the optimal attention pattern per attention head in VLMs using an offline characterization flow.
- Implemented an efficient sparse attention kernel to leverage BlindSight’s sparsity patterns.
- Investigated the underlying source of this sparsity, emphasizing the role of modality boundary tokens. This motivates an efficient VLM design composed of a mixture of sparse and dense attention layers.

2 RELATED WORK

Static Attention Sparsity in LLMs: Static post-training optimizations rely on offline characterization to identify fixed sparsity patterns to be used during inference. The sliding window attention layer introduced in LongFormers Beltagy et al. (2020) computed the attention using only the most recent keys per query. Sparse Transformer Child et al. (2019) employs a strided pattern along with windowing for efficient computation. Big Bird Zaheer et al. (2021) enhances the sliding window approach by incorporating random blocks to capture block sparsity. Streaming LLM Xiao et al. (2024b) highlighted the role of sink tokens, early tokens that garner high attention scores Vig & Belinkov (2019). This insight can be used to confine the computation to an A-shaped segment of the overall attention. While static sparsity patterns generally result in coherent conversations and efficient computation, they show poor performance on LLM benchmarks.

Dynamic Attention Sparsity in LLMs: Dynamic sparsity techniques rely on additional inference-time metrics to derive an input-dependent attention sparsity mask. DuoAttention Xiao et al. (2024a) seeks to address gaps in static sparsity by classifying attention heads into streaming heads (A-shaped) and retrieval heads (full attention) through fine-tuning. SnapKV Li et al. (2024) proposes compressing the KV cache by selecting out clustered KV positions for each head. MInference Jiang et al. (2024b) proposes to categorize each head during inference into three types: A-shaped, block sparse and vertical-slash; though the vertical-slash pattern proves to be sufficient in practice. Furthermore, attention sparsity is also observed in the KV cache during the decode phase. Techniques such as H2O Zhang et al. (2023), ScissorHands Liu et al. (2023) and PyramidKV Cai et al. (2025) prune past tokens using attention score-based metrics.

Sparsity in VLMs: MInference Li et al. (2025) dynamically derives intra-modality sparse patterns, similar to MInference, augmenting them with static cross-modality sparsity patterns derived for video inputs. The identification of static sparsity patterns per head is conducted offline on a single sample. However, online computation is required to identify the intra-modality grid-like sparsity pattern. LookM Wan et al. (2024) optimizes the KV cache for VLMs using a KV cache merging scheme. VAR Kang et al. (2025) identifies visual attention sinks in single-image scenarios.

Token Compression in VLMs: Token compression techniques use attention scores or token similarity to prune or merge redundant visual tokens Chen et al. (2024a); Alvar et al. (2025); Shang et al. (2024); Wen et al. (2025); Gong et al. (2024). Token compression approaches focus on reducing the number of tokens, and do not target the inherent sparsity available in attention computation in VLMs. This results in quadratic computation complexity, compared to the sub-quadratic complexity offered by BlindSight. BlindSight can be combined with token compression to further reduce computation in VLMs (Section 6.3, Appendix J).

3 ATTENTION SPARSITY IN VLMs

3.1 ATTENTION PRELIMINARIES

The scaled dot product attention utilized in the Multi-Head Attention layers Vaswani et al. (2023) models the interactions of tokens within a sequence without relying on recurrence. We focus here specifically on the prefill stage. Given an input sequence of length L and a model with hidden dimension d_h , linear projection layers first derive the query Q , key K and value V matrices; each with dimensions $L \times d_k$. The attention operation is then defined as:

$$\text{Attn}(Q, K, V) = \text{SoftMax} \left(\frac{QK^T}{\sqrt{d_k}} + \text{Mask} \right) V$$

During the prefill stage, the causal attention mask is used to prevent the interaction of a text token with future tokens. There is however a lack of standardization in the attention mechanism for the image component of a prompt, with either non-causal or causal masks used in different models. In this paper, we refer to a VLM’s default attention mask as the dense mask. By convention, $\text{SoftMax}(QK^T/\sqrt{d_k} + Mask)$ is referred to as the *attention matrix*.

3.2 SPARSITY CATEGORIZATION

With a specific focus on inter-image interactions, we visually studied the attention matrix across layers for a variety of inputs. Although precise conclusions on sparsity patterns can only be derived by studying the attention output, the attention matrix provides a visual proxy for analysis. Fig. 2 represents examples of the attention matrix for different types of sparse heads in Qwen2-VL Wang et al. (2024b). We observe that these patterns remain consistent across other open-source VLMs (Appendix A). We observe that attention heads in VLMs belong to two categories, **Dense Heads** and **Sparse Heads**.

- **Dense Heads** have no discernible pattern of low-valued elements in the attention matrix, or they consist of patterns that are not repeated across models and layers.
- **Sparse Heads** have many low-valued elements, and exhibit distinct boundaries at the text-image and image-image interface. They can be broadly categorized into three groups: **Sink Heads**, **Intra-Image Heads** and **Intra-Image+Sink Heads**.

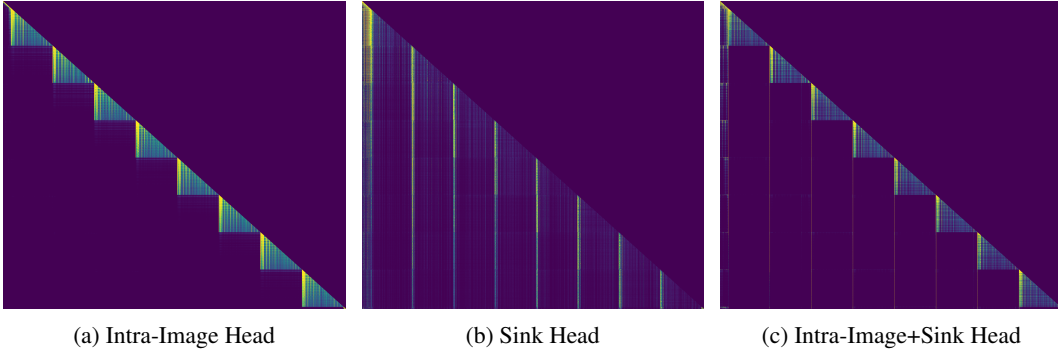


Figure 2: Sparse attention categories in VLMs for prompts with multiple images

We further observe that variations exist in the sparsity patterns for sparse heads with different inputs. Further analysis of sparse heads reveals that text-to-image or image-to-image transitions are frequently followed by an attention sink Xiao et al. (2024b). **Sink Heads** exhibit only this attention-sink behavior, with no intra-image attention. **Intra-Image Heads** only attend within each image, with no sink-based cross-image attention. These heads focus mostly on intra-image processing. **Intra-Image+Sink Heads** combine both the attention sink and intra-image pattern per image. Across all these scenarios, the text tokens continue to attend to all the previous tokens, leading to horizontal and vertical bands in the attention matrix. These sparsity categories offer a template for creating a mask based on the positions of the text and image tokens in the prompt. Note that the model’s original attention approach (dense attention) can be used to handle non-sparse heads.

We exploit the inherent sparsity in VLMs by masking computations in attention heads that contribute negligibly to the final attention output. BlindSight optimizes inter-image attentions, and its impact is particularly relevant in multi-image scenarios (Fig. 1b). The impact of optimizing intra-image attentions Li et al. (2025) appears relatively modest for longer contexts dominated by inter-image attentions (Fig. 1b). We specifically focus on inputs containing multiple images rather than videos, as most models lack per-frame delimiters for videos, crucial for VLM sparsity (Section 7). The exception here is Qwen3-VL, which has introduced per-frame delimiters for videos, inducing sparsity which BlindSight can exploit (Appendix K).

4 BLINDSIGHT

BlindSight consists of two steps: prompt-level characterization and dataset-level aggregation. The first step involves characterizing attention heads for a single prompt. Here, we aim to identify the optimal sparsity pattern from the four categories. Given variations in the mapping for different prompts, we derive a single attention head to attention-type mapping across a characterization dataset by aggregating prompt-level categorizations.

4.1 PROMPT-LEVEL CHARACTERIZATION

Although visual characterization can provide valuable insights, practical deployments require an algorithmic approach to determine the optimal attention sparsity pattern. BlindSight addresses this need by minimizing the difference between the baseline dense attention output and the proposed sparse attention at every attention head. Algorithm 1 describes the approach in detail. Every sparsity pattern is associated with a sparsity mask to compute the attention. Aligning the outputs at each attention head ensures that the overall model remains aligned. A threshold α_{layer} on the normalized mean squared error (NMSE) serves as the selection criterion. The algorithm prioritizes patterns that achieve the lowest theoretical FLOPs. We revert to the original dense pattern when no sparse attention achieves an NMSE below α_{layer} .

Algorithm 1 BlindSight: Prompt-level Characterization

Input: layer; head; $Q, K, V \in \mathcal{R}^{L \times d_k}$; α_{layer}
Output: head_type[layer][head]
 $\text{Attn}_{\text{ref}} = \text{SoftMax} \left(\frac{QK^T}{\sqrt{d_k}} + \text{DenseMask} \right) V$
head_type[layer][head] = 'Dense Head'
for mask \in ['Sink Head', 'Intra-Image Head', 'Intra-Image+Sink Head'] **do**
 $\text{Attn}_{\text{mask}} = \text{SoftMax} \left(\frac{QK^T}{\sqrt{d_k}} + \text{mask} \right) V$
 $\text{NMSE}_{\text{mask}} = \|\text{Attn}_{\text{mask}} - \text{Attn}_{\text{ref}}\|_2^2 / \|\text{Attn}_{\text{ref}}\|_2^2$
 if $\text{NMSE}_{\text{mask}} < \alpha_{layer}$ **then**
 head_type[layer][head] = mask
 break
 end if
end for
return head_type[layer][head]

4.2 DATASET-LEVEL AGGREGATION

We repeat the prompt-level characterization on a dataset to investigate the variation in masks selected for different prompts. For this characterization, we use the Multimodal Multi-image Understanding (MMIU) benchmark Meng et al. (2024), which is designed to evaluate multi-image comprehension. We observe that most layers exhibit a preference for a single dominant attention pattern. In certain layers, however, we observe that the dense pattern is preferred for a non-negligible fraction, even though it is not the predominant choice. Detailed results on the sparsity pattern selected across layers are discussed in Appendix B.

We propose an empirical rule-based aggregation algorithm based on the distribution of the attention pattern across prompts. For every layer, we rely on the predominant attention pattern selected across the dataset, with the exception of instances where the Dense pattern exceeds a specified threshold fraction. This cautious strategy mitigates potential performance degradations associated with excessive sparsification. In scenarios where neither the Sink nor the Intra-Image pattern dominates, we revert to the Intra-Image+Sink category. As shown in Fig. 3, we observe that 60% of the layers tend to be sparse across Qwen-type models. Note that MMIU is chosen for offline characterization due to the variety of tasks contained within this benchmark. However, the proposed approach can be used with other datasets for characterization (Appendix H).

Algorithm 2 BlindSight: Dataset-level Aggregation

```
Input: layer; head; head_type_fraction;  $\gamma_d$ ;  $\gamma_s$ ;  $\gamma_i$   
if head_type_fraction[layer][head]['Dense'] >  $\gamma_d$  then  
    return 'Dense'  
end if  
if head_type_fraction[layer][head]['Sink'] >  $\gamma_s$  then  
    return 'Sink'  
end if  
if head_type_fraction[layer][head]['Intra-Image'] >  $\gamma_i$  then  
    return 'Intra-Image'  
else  
    return 'Intra-Image+Sink'  
end if
```

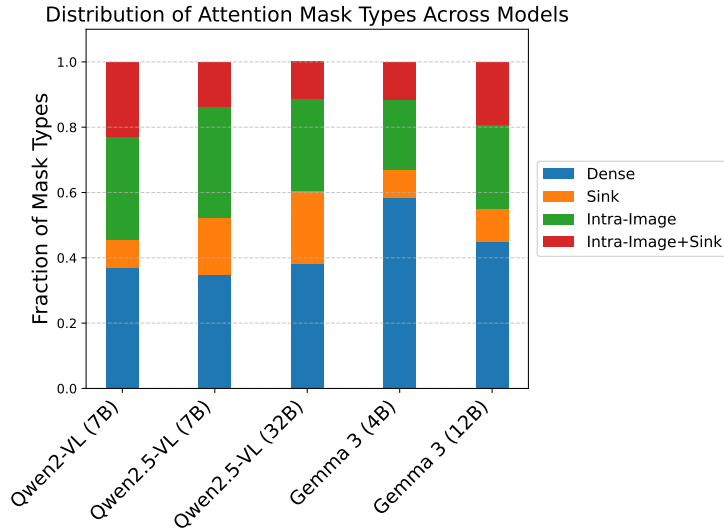
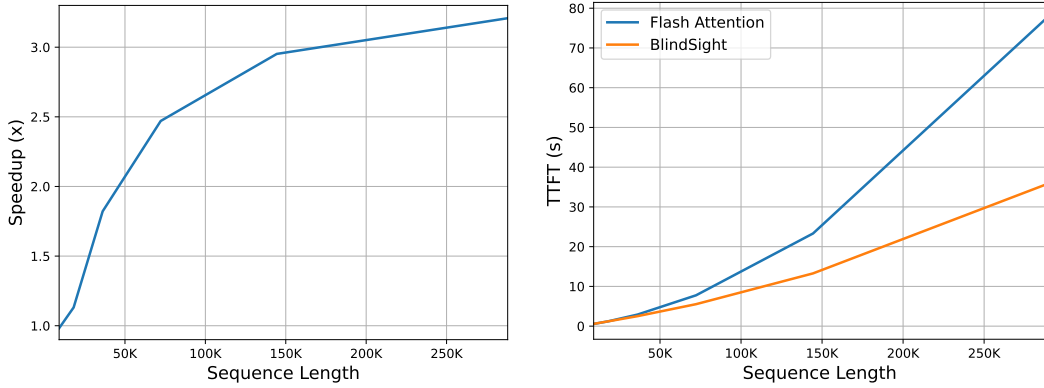


Figure 3: Distribution of sparsity categories across VLMs

5 BLINDSIGHT SPARSE ATTENTION KERNEL

We develop a Triton-based GPU compute kernel (Tillet et al., 2019) for BlindSight that efficiently exploits the sparsity patterns identified in VLMs. Following Flash Attention (Dao et al., 2022), the BlindSight kernel partitions the attention computation into tiles (contiguous chunks of queries, keys and values) and computes the attention within each tile. We implement four subroutines, each optimized for different scenarios within a tile. The primary distinction between subroutines lies in their mask construction logic. During runtime, the appropriate subroutine is selected based on the attention-head type and the presence of text or image tokens in the tile. The kernel receives the attention head type, the tile indices, and the text/image token boundaries (for the query, key dimensions) to construct the attention mask. Completely sparse tiles are skipped. Appendix L provides further details on the kernel, including subroutines and optimizations.

We demonstrate performance gains by integrating the BlindSight kernel into the Qwen 2.5-VL (7B) model (Setup per Section 6.1). Fig. 4a illustrates the latency improvements of the kernel compared to the Triton-based Flash Attention kernel over different sequence lengths, across only the attention layers. The kernel achieves increased speedup as the context length increases (i.e., as the number of images grows), due to increased sparsity. However, at very long sequence lengths, the $O(N^2)$ complexity of the dense heads begins to manifest itself through plateauing gains. Fig. 4b reveals the overall impact using the BlindSight kernel. The TTFT is improved $2.2\times$ at a sequence length of 300K. Bottlenecks in other modules masks the attention level gains. BlindSight exhibits a nearly linear trend in TTFT with sequence length, in contrast to the quadratic trend without sparsity.



(a) BlindSight-based attention speedup over layers (b) TTFT Comparison: Flash Attention vs BlindSight

Figure 4: BlindSight Kernel: Performance improvements in Qwen 2.5-VL (7B)

6 EVALUATION

We evaluate BlindSight on different VLMs using benchmarks for multi-image comprehension. This section first provides details on the experimental setup, models and benchmarks. We compare the accuracies of the original and sparsified models. We also highlight BlindSight’s compatibility with alternate VLM optimization techniques such as token pruning.

6.1 EXPERIMENTAL SETUP

Models We use open-source models available through Hugging Face Wolf et al. (2020) to implement our proposed solution. The experiments focus on Qwen2-VL (7B) Wang et al. (2024b), Qwen2.5-VL (7B, 32B) Bai et al. (2025b), and Gemma 3 (4B, 12B) Gemma team (2025). All of these models include a large transformer-based decoder module to jointly process vision embeddings (derived from a vision encoder) and text embeddings.

Implementation We utilize attention mechanisms specific to each model within the Hugging Face Transformers library Wolf et al. (2020) to develop a custom attention mask variant. This custom sparse attention layer is integrated into the base model via monkey-patching. While the characterization stage uses a native PyTorch-based Paszke et al. (2019) implementation, the BlindSight kernel is used for inference.

Sparse Mask Generation: The sparse attention mask template requires knowledge of the positions of text and images within the prompt. These positions are determined by identifying the `<vision_start>` and `<vision_end>` tokens within the tokenized prompt. Each category of sparse mask employs a different implementation based on these positions. The attention sink for every image is set to 10% of the corresponding image length. Note that in this work, we only aim to optimize prefill time for VLMs and retain the entire KV cache.

The position of attention sinks in the sparse layers depends upon the specific implementation and training recipe used in the model. For typical VLMs such as the Qwen family, the attention sinks always occur at the start of the image. Gemma 3 tokenizes every image to the same length and employs a non-causal attention mechanism within an image. The attention sinks here occur at fixed locations within every image as shown in Fig. 8. We identified the locations of the attention sinks using the MMIU dataset Meng et al. (2024), and selected the top-10% with the highest frequency.

Infrastructure: The experiments were carried out on an AMD Instinct MI300X node with 8 GPUs. We utilized a PyTorch container with ROCm installed. We were able to load the entire model onto a single GPU for visual analysis and performance evaluation.

Hyperparameter Selection: Hyperparameters (α_{layer} , γ_d , γ_s) can be used to trade off sparsity and accuracy (Details available in Appendix D.3). For typical VLMs with causal intra-image attention that display sparsity patterns similar to Fig. 2 (Qwen2-VL, Qwen2.5-VL, Qwen3-VL, Llama 4),

we recommend using a fixed $\alpha_{layer} = 0.1$, $\gamma_d = 0.25$ and $\gamma_s = 0.60$. For atypical models such as Gemma 3 (non-causal intra-image attention), we recommend a Linear α_{layer} scheme. α_{layer} and γ_d are the key hyperparameters that controls the accuracy-sparsity trade-off. γ_s does not significantly impact the accuracy. We provide detailed ablation studies on the hyperparameters in Appendix D.

Benchmarks: BlindSight is a prefill optimization strategy that specifically impacts scenarios involving image-to-image interactions. We evaluate BlindSight using a variety of multi-image understanding benchmarks such as MMIU Meng et al. (2024), MuirBench Wang et al. (2024a), MANTIS Jiang et al. (2024a), MIRB Zhao et al. (2024), MMT-Bench Ying et al. (2024) and MMIE Xia et al. (2024). These cover a broad spectrum of perceptual, relational, retrieval and reasoning tasks; including spatial and temporal reasoning, visual analogy, attribute matching, multi-hop logic, OCR and diagram understanding. These benchmarks present a sequence of images accompanied by a multiple-choice question or reasoning task (Details in Appendix E). For the MMIE benchmark, we specifically evaluate the multi-step reasoning (MSR) task.

6.2 EVALUATION ON BENCHMARKS

The results shown in Table 1 highlight the minimal performance degradation from sparsifying a model using BlindSight. We compare the performance of BlindSight with sparse models in which every attention head is replaced with a sparse head category. Typically, BlindSight’s accuracy degradations are marginal, suggesting that a large portion of masked-out computations have minimal impact on the final prediction. We highlight the FLOPs saved in Appendix G. Independent of the task at hand, the evaluated VLMs were observed to think through before responding. The decode phase remains coherent despite the sparsity enforced in the prefill phase (Examples in Appendix F).

We note that a model comprising a mixture of sparse and dense attention heads, derived using BlindSight, consistently outperforms an all-sparse model. This suggests that full inter-image attention in dense heads and partial inter-image attention through sinks is sufficient to maintain performance on complex multi-image comprehension tasks. Among the sparse model evaluations, models using only attention sinks perform consistently worse. Finally, we also observe that BlindSight offers robustness to characterization datasets beyond MMIU (Appendix H), while also maintaining consistent performance across image tokenization lengths (Appendix I).

The focus of this paper is limited to multi-image benchmarks, due to the lack of BlindSight-like sparsity for video inputs in most current models. This is related to the absence of delimiter tokens, discussed in Section 7. Qwen3-VL Bai et al. (2025a) introduced a per-frame delimiter for video inputs. We have included an evaluation on the VideoMME Fu et al. (2025) benchmark in Appendix K with BlindSight showing a 0.76% accuracy degradation. We aim to study extensions of BlindSight to videos in the future.

6.3 COMPATIBILITY WITH TOKEN COMPRESSION

Token compression and pruning offer alternate approaches to optimize VLMs. We conducted a limited study on the impact of token pruning using DivPrune Alvar et al. (2025) and observe that sparsity patterns are retained even with 90% of the tokens pruned away. Details are provided in Appendix J. BlindSight is expected to be orthogonal to these techniques and can be combined to further reduce attention computation. Table 2 shows that combining BlindSight with 90% and 75% token compression still results in accuracy within 2% of DivPrune on Qwen2-VL (7B).

7 DISCUSSION

Attention sinks emerge in LLMs during pre-training, where the SoftMax operator is repeatedly applied on the early tokens Xiao et al. (2024b). Additionally, massive activations occur independent of input data within specific attention layers. These activations develop into sinks that function as implicit bias terms within the attention layer Sun et al. (2024). Furthermore, delimiter tokens (punctuation, \n) with low semantic value often correspond to high attention scores Clark et al. (2019). Gu et al. (2025); Barbero et al. (2025) highlights the role of the sink in long-context learning.

We now empirically study the role of attention sinks associated with every image. VLM prompts typically consist of delimiter tokens at the start (<vision_start>) and end (<vision_end>) of

Qwen2-VL (7B)						
	MMIU	MANTIS	MuirBench	MIRB	MMT	MMIE
Original	34.12	61.61	49.83	70.77	63.17	70.20
All Sink Heads	33.61	60.19	42.57	66.89	61.58	67.12
All Intra-Image Heads	34.90	57.35	43.95	67.83	62.67	69.91
All Intra-Image+Sink Heads	34.12	62.56	47.45	69.22	62.69	70.05
BlindSight ($\alpha_{layer} = 0.1$)	34.90	63.03	48.86	69.61	63.13	70.00
Qwen2.5-VL (7B)						
	MMIU	MANTIS	MuirBench	MIRB	MMT	MMIE
Original	35.51	68.25	55.31	71.12	61.29	71.25
All Sink Heads	30.54	62.56	47.29	69.21	60.41	67.93
All Intra-Image Heads	31.83	54.98	47.64	69.98	61.22	70.13
All Intra-Image+Sink Heads	34.23	62.09	51.33	70.01	61.27	70.21
BlindSight ($\alpha_{layer} = 0.1$)	35.06	66.35	53.75	70.30	61.35	70.83
Qwen2.5-VL (32B)						
	MMIU	MANTIS	MuirBench	MIRB	MMT	MMIE
Original	44.67	72.51	61.87	73.37	65.85	78.28
All Sink Heads	35.60	64.93	42.80	68.89	63.04	74.20
All Intra-Image Heads	38.19	58.77	49.14	71.9	65.21	76.92
All Intra-Image+Sink Heads	37.58	67.77	56.19	72.11	65.32	77.21
BlindSight ($\alpha_{layer} = 0.1$)	44.10	70.62	61.64	72.39	65.42	77.80
Gemma 3 (4B)						
	MMIU	MANTIS	MuirBench	MIRB	MMT	MMIE
Original	33.78	63.51	35.39	53.83	54.63	60.96
All Sink Heads	29.44	46.08	24.23	35.22	43.46	46.05
All Intra-Image Heads	34.44	49.77	29.77	40.17	54.56	58.52
All Intra-Image+Sink Heads	33.17	50.69	27.83	42.67	52.33	57.48
BlindSight (Linear α_{layer})	35.01	60.19	33.93	51.34	54.76	60.93
Gemma 3 (12B)						
	MMIU	MANTIS	MuirBench	MIRB	MMT	MMIE
Original	35.81	69.67	50.64	54.97	58.73	62.93
All Sink Heads	27.61	55.76	29.65	39.66	43.46	47.17
All Intra-Image Heads	33.67	57.58	41.19	43.9	57.95	59.80
All Intra-Image+Sink Heads	32.61	60.37	37.88	44.59	56.09	57.00
BlindSight (Linear α_{layer})	33.95	68.25	46.78	53.76	59.83	62.62

Table 1: Accuracy (%) on multi-image comprehension benchmarks

every image. These image boundary tokens are essential for enabling sparsity. To support this claim, we study attention patterns removing these boundary tokens in a text-image interleaved prompt in Qwen2-VL (7B). We observe that the intra-image attention ceases to exist (Fig. 5). Partial information pooling across images still persists via weak sinks, resulting in incoherent responses.

In current pre-processing schemes, videos are decomposed into images, with the entire video segment in the prompt enclosed by a single pair of delimiter tokens. In multi-image settings however, each image is enclosed by its own pair of delimiter tokens. The absence of sparsity currently for video inputs is explained by the lack of per-frame delimiter tokens. In line with our observation, Qwen3-VL introduced per frame delimiter tokens along with temporal markers, inducing attention sparsity for video inputs (Appendix K).

Model	Pruning	MMIU	MANTIS	MuirBench
Baseline	-	34.12	61.61	49.83
BlindSight	-	34.90	63.03	48.86
DivPrune (DP)	90%	33.78	58.77	45.33
BlindSight + DP	90%	34.38	60.00	44.59
DivPrune (DP)	75%	34.17	59.72	48.09
BlindSight + DP	75%	35.46	60.36	46.39

Table 2: Qwen2-VL (7B) performance with token compression.

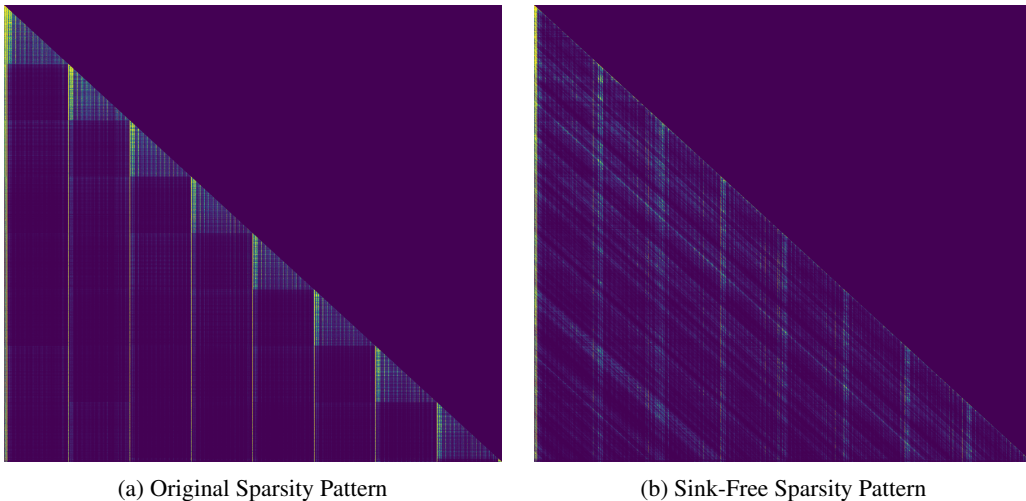


Figure 5: Impact of removing image boundary tokens: Removing `<image_start>` and `<image_end>` impairs attention sinks and disrupts the intra-image masking pattern.

While BlindSight is a post-training VLM optimization technique, we advocate for incorporating such sparsity during training into the model architecture itself. Llama 4 Meta AI (2025) includes chunked attention (document masking) layers, which also enable linear scaling in complexity at long sequence lengths. Native Sparse Attention Yuan et al. (2025) and DeepSeek Sparse Attention DeepSeek-AI (2025) directly incorporate dynamic sparsity into the attention mechanism. Performant models can be composed through a mixture of low-complexity attention layers and dense attention layers, as evidenced by Table 1. Post-training sparsification Xiao et al. (2024a) and hybrid state-space based models Glorioso et al. (2024); Ren et al. (2025); Yang et al. (2025) highlight the potential to achieve improved efficiency and performance by strategically combining sparse, linear and dense attention mechanisms.

8 CONCLUSION

We investigated inter-image interactions within the attention layers of VLMs. From this analysis, we developed BlindSight: an input-template-based VLM sparsification technique that achieves performance levels comparable to the original dense attention across various multi-image understanding benchmarks. We developed a Triton-based kernel that showcased performance gains. We finally presented an empirical analysis on the origin of sparsity in VLMs with multi-image inputs. We observe consistent sparsity patterns across a wide range of models, tasks, and tokenization approaches. We anticipate that these findings will motivate future research to natively integrate hybrid sparse and dense attention mechanisms into VLM architectures.

REFERENCES

- Saeed Ranjbar Alvar, Gursimran Singh, Mohammad Akbari, and Yong Zhang. Divprune: Diversity-based visual token pruning for large multimodal models, 2025. URL <https://arxiv.org/abs/2503.02175>.
- Shuai Bai, Yuxuan Cai, Ruizhe Chen, Keqin Chen, Xionghui Chen, Zesen Cheng, Lianghao Deng, Wei Ding, Chang Gao, Chunjiang Ge, Wenbin Ge, Zhifang Guo, Qidong Huang, Jie Huang, Fei Huang, Binyuan Hui, Shutong Jiang, Zhaohai Li, Mingsheng Li, Mei Li, Kaixin Li, Zicheng Lin, Junyang Lin, Xuejing Liu, Jiawei Liu, Chenglong Liu, Yang Liu, Dayiheng Liu, Shixuan Liu, Dunjie Lu, Ruilin Luo, Chenxu Lv, Rui Men, Lingchen Meng, Xuancheng Ren, Xingzhang Ren, Sibao Song, Yuchong Sun, Jun Tang, Jianhong Tu, Jianqiang Wan, Peng Wang, Pengfei Wang, Qiuyue Wang, Yuxuan Wang, Tianbao Xie, Yiheng Xu, Haiyang Xu, Jin Xu, Zhibo Yang, Mingkun Yang, Jianxin Yang, An Yang, Bowen Yu, Fei Zhang, Hang Zhang, Xi Zhang, Bo Zheng, Humen Zhong, Jingren Zhou, Fan Zhou, Jing Zhou, Yuanzhi Zhu, and Ke Zhu. Qwen3-vl technical report. *arXiv preprint arXiv:2511.21631*, 2025a.
- Shuai Bai, Keqin Chen, Xuejing Liu, Jialin Wang, Wenbin Ge, Sibao Song, Kai Dang, Peng Wang, Shijie Wang, Jun Tang, Humen Zhong, Yuanzhi Zhu, Mingkun Yang, Zhaohai Li, Jianqiang Wan, Pengfei Wang, Wei Ding, Zheren Fu, Yiheng Xu, Jiabo Ye, Xi Zhang, Tianbao Xie, Zesen Cheng, Hang Zhang, Zhibo Yang, Haiyang Xu, and Junyang Lin. Qwen2.5-VL Technical Report, 2025b. URL <https://arxiv.org/abs/2502.13923>.
- Federico Barbero, Álvaro Arroyo, Xiangming Gu, Christos Perivolaropoulos, Michael Bronstein, Petar Veličković, and Razvan Pascanu. Why do LLMs attend to the first token?, 2025. URL <https://arxiv.org/abs/2504.02732>.
- Iz Beltagy, Matthew E. Peters, and Arman Cohan. Longformer: The Long-Document Transformer, 2020. URL <https://arxiv.org/abs/2004.05150>.
- Gagan Bhatia, El Moatez Billah Nagoudi, Hasan Cavusoglu, and Muhammad Abdul-Mageed. FinTral: A Family of GPT-4 Level Multimodal Financial Large Language Models, 2024. URL <https://arxiv.org/abs/2402.10986>.
- Kevin Black, Noah Brown, Danny Driess, Adnan Esmail, Michael Equi, Chelsea Finn, Niccolo Fusai, Lachy Groom, Karol Hausman, Brian Ichter, Szymon Jakubczak, Tim Jones, Liyiming Ke, Sergey Levine, Adrian Li-Bell, Mohith Mothukuri, Suraj Nair, Karl Pertsch, Lucy Xiaoyang Shi, James Tanner, Quan Vuong, Anna Walling, Haohuan Wang, and Ury Zhilinsky. π_0 : A Vision-Language-Action Flow Model for General Robot Control, 2024. URL <https://arxiv.org/abs/2410.24164>.
- William Brandon, Aniruddha Nrusimha, Kevin Qian, Zachary Ankner, Tian Jin, Zhiye Song, and Jonathan Ragan-Kelley. Striped Attention: Faster Ring Attention for Causal Transformers, 2023. URL <https://arxiv.org/abs/2311.09431>.
- Anthony Brohan, Noah Brown, Justice Carbajal, Yevgen Chebotar, Xi Chen, Krzysztof Choromanski, Tianli Ding, Danny Driess, Avinava Dubey, Chelsea Finn, Pete Florence, Chuyuan Fu, Montse Gonzalez Arenas, Keerthana Gopalakrishnan, Kehang Han, Karol Hausman, Alexander Herzog, Jasmine Hsu, Brian Ichter, Alex Irpan, Nikhil Joshi, Ryan Julian, Dmitry Kalashnikov, Yuheng Kuang, Isabel Leal, Lisa Lee, Tsang-Wei Edward Lee, Sergey Levine, Yao Lu, Henryk Michalewski, Igor Mordatch, Karl Pertsch, Kanishka Rao, Krista Reymann, Michael Ryoo, Grecia Salazar, Pannag Sanketi, Pierre Sermanet, Jaspiar Singh, Anikait Singh, Radu Soricut, Huang Tran, Vincent Vanhoucke, Quan Vuong, Ayzaan Wahid, Stefan Welker, Paul Wohlhart, Jialin Wu, Fei Xia, Ted Xiao, Peng Xu, Sichun Xu, Tianhe Yu, and Brianna Zitkovich. RT-2: Vision-Language-Action Models Transfer Web Knowledge to Robotic Control, 2023. URL <https://arxiv.org/abs/2307.15818>.
- Zefan Cai, Yichi Zhang, Bofei Gao, Yuliang Liu, Yucheng Li, Tianyu Liu, Keming Lu, Wayne Xiong, Yue Dong, Junjie Hu, and Wen Xiao. PyramidKV: Dynamic KV Cache Compression based on Pyramidal Information Funneling, 2025. URL <https://arxiv.org/abs/2406.02069>.

-
- Liang Chen, Haozhe Zhao, Tianyu Liu, Shuai Bai, Junyang Lin, Chang Zhou, and Baobao Chang. An image is worth 1/2 tokens after layer 2: Plug-and-play inference acceleration for large vision-language models, 2024a. URL <https://arxiv.org/abs/2403.06764>.
- Zhe Chen, Jiannan Wu, Wenhai Wang, Weijie Su, Guo Chen, Sen Xing, Muyan Zhong, Qinglong Zhang, Xizhou Zhu, Lewei Lu, Bin Li, Ping Luo, Tong Lu, Yu Qiao, and Jifeng Dai. InternVL: Scaling up Vision Foundation Models and Aligning for Generic Visual-Linguistic Tasks, 2024b. URL <https://arxiv.org/abs/2312.14238>.
- Rewon Child, Scott Gray, Alec Radford, and Ilya Sutskever. Generating Long Sequences with Sparse Transformers, 2019. URL <https://arxiv.org/abs/1904.10509>.
- Kevin Clark, Urvashi Khandelwal, Omer Levy, and Christopher D. Manning. What Does BERT Look At? An Analysis of BERT’s Attention, 2019. URL <https://arxiv.org/abs/1906.04341>.
- Tri Dao, Daniel Y. Fu, Stefano Ermon, Atri Rudra, and Christopher Ré. Flashattention: Fast and memory-efficient exact attention with io-awareness, 2022. URL <https://arxiv.org/abs/2205.14135>.
- DeepSeek-AI. Deepseek-v3.2-exp: Boosting long-context efficiency with deepseek sparse attention, 2025.
- Jean-benoit Delbrouck, Khaled Saab, Maya Varma, Sabri Eyuboglu, Pierre Chambon, Jared Dunmon, Juan Zambrano, Akshay Chaudhari, and Curtis Langlotz. ViLMedic: a framework for research at the intersection of vision and language in medical AI. In *Proceedings of the 60th Annual Meeting of the Association for Computational Linguistics: System Demonstrations*, pp. 23–34, Dublin, Ireland, May 2022. Association for Computational Linguistics. URL <https://aclanthology.org/2022.acl-demo.3>.
- Chaoyou Fu, Yuhan Dai, Yongdong Luo, Lei Li, Shuhuai Ren, Renrui Zhang, Zihan Wang, Chenyu Zhou, Yunhang Shen, Mengdan Zhang, et al. Video-mme: The first-ever comprehensive evaluation benchmark of multi-modal llms in video analysis. In *CVPR*, 2025.
- Gemma team. Gemma 3 Technical Report, 2025. URL <https://arxiv.org/abs/2503.19786>.
- Paolo Glorioso, Quentin Anthony, Yury Tokpanov, James Whittington, Jonathan Pilault, Adam Ibrahim, and Beren Millidge. Zamba: A Compact 7B SSM Hybrid Model, 2024. URL <https://arxiv.org/abs/2405.16712>.
- Ruihao Gong, Yang Yong, Shiqiao Gu, Yushi Huang, Chengtao Lv, Yunchen Zhang, Dacheng Tao, and Xianglong Liu. Llmc: Benchmarking large language model quantization with a versatile compression toolkit. In *EMNLP (Industry Track)*, pp. 132–152, 2024. URL <https://aclanthology.org/2024.emnlp-industry.12>.
- Xiangming Gu, Tianyu Pang, Chao Du, Qian Liu, Fengzhuo Zhang, Cunxiao Du, Ye Wang, and Min Lin. When Attention Sink Emerges in Language Models: An Empirical View, 2025. URL <https://arxiv.org/abs/2410.10781>.
- Iryna Hartsock and Ghulam Rasool. Vision-language models for medical report generation and visual question answering: a review. *Frontiers in Artificial Intelligence*, 7, November 2024. ISSN 2624-8212. doi: 10.3389/frai.2024.1430984. URL <http://dx.doi.org/10.3389/frai.2024.1430984>.
- Anthony Hu, Lloyd Russell, Hudson Yeo, Zak Murez, George Fedoseev, Alex Kendall, Jamie Shotton, and Gianluca Corrado. GAIA-1: A Generative World Model for Autonomous Driving, 2023. URL <https://arxiv.org/abs/2309.17080>.
- Dongfu Jiang, Xuan He, Huaye Zeng, Cong Wei, Max Ku, Qian Liu, and Wenhui Chen. MAN-TIS: Interleaved Multi-Image Instruction Tuning, 2024a. URL <https://arxiv.org/abs/2405.01483>.

-
- Huiqiang Jiang, Yucheng Li, Chengruidong Zhang, Qianhui Wu, Xufang Luo, Surin Ahn, Zhenhua Han, Amir H. Abdi, Dongsheng Li, Chin-Yew Lin, Yuqing Yang, and Lili Qiu. MInference 1.0: Accelerating Pre-filling for Long-Context LLMs via Dynamic Sparse Attention, 2024b. URL <https://arxiv.org/abs/2407.02490>.
- Seil Kang, Jinyeong Kim, Junhyeok Kim, and Seong Jae Hwang. See what you are told: Visual attention sink in large multimodal models, 2025. URL <https://arxiv.org/abs/2503.03321>.
- Yucheng Li, Huiqiang Jiang, Chengruidong Zhang, Qianhui Wu, Xufang Luo, Surin Ahn, Amir H. Abdi, Dongsheng Li, Jianfeng Gao, Yuqing Yang, and Lili Qiu. MMInference: Accelerating Pre-filling for Long-Context VLMs via Modality-Aware Permutation Sparse Attention, 2025. URL <https://arxiv.org/abs/2504.16083>.
- Yuhong Li, Yingbing Huang, Bowen Yang, Bharat Venkitesh, Acyr Locatelli, Hanchen Ye, Tianle Cai, Patrick Lewis, and Deming Chen. SnapKV: LLM Knows What You are Looking for Before Generation, 2024. URL <https://arxiv.org/abs/2404.14469>.
- Hao Liu, Matei Zaharia, and Pieter Abbeel. RingAttention with Blockwise Transformers for Near-Infinite Context. In *The Twelfth International Conference on Learning Representations*, 2024. URL <https://openreview.net/forum?id=WsRHpHH4s0>.
- Zichang Liu, Aditya Desai, Fangshuo Liao, Weitao Wang, Victor Xie, Zhaozhuo Xu, Anastasios Kyrillidis, and Anshumali Shrivastava. Scissorhands: Exploiting the Persistence of Importance Hypothesis for LLM KV Cache Compression at Test Time, 2023. URL <https://arxiv.org/abs/2305.17118>.
- Fanqing Meng, Jin Wang, Chuanhao Li, Quanfeng Lu, Hao Tian, Jiaqi Liao, Xizhou Zhu, Jifeng Dai, Yu Qiao, Ping Luo, Kaipeng Zhang, and Wenqi Shao. MMIU: Multimodal Multi-image Understanding for Evaluating Large Vision-Language Models, 2024. URL <https://arxiv.org/abs/2408.02718>.
- Meta AI. Llama 4 Models: Model Card and Documentation, 2025. URL https://github.com/meta-llama/llama-models/blob/main/models/llama4/MODEL_CARD.md.
- Niklas Muennighoff, Zitong Yang, Weijia Shi, Xiang Lisa Li, Li Fei-Fei, Hannaneh Hajishirzi, Luke Zettlemoyer, Percy Liang, Emmanuel Candès, and Tatsunori Hashimoto. s1: Simple test-time scaling, 2025. URL <https://arxiv.org/abs/2501.19393>.
- Adam Paszke, Sam Gross, Francisco Massa, Adam Lerer, James Bradbury, Gregory Chanan, Trevor Killeen, Zeming Lin, Natalia Gimelshein, Luca Antiga, Alban Desmaison, Andreas Köpf, Edward Yang, Zach DeVito, Martin Raison, Alykhan Tejani, Sasank Chilamkurthy, Benoit Steiner, Lu Fang, Junjie Bai, and Soumith Chintala. PyTorch: An Imperative Style, High-Performance Deep Learning Library, 2019. URL <https://arxiv.org/abs/1912.01703>.
- Liliang Ren, Yang Liu, Yadong Lu, Yelong Shen, Chen Liang, and Weizhu Chen. Samba: Simple Hybrid State Space Models for Efficient Unlimited Context Language Modeling, 2025. URL <https://arxiv.org/abs/2406.07522>.
- Ranajoy Sadhukhan, Zhuoming Chen, Haizhong Zheng, Yang Zhou, Emma Strubell, and Beidi Chen. Kinetics: Rethinking Test-Time Scaling Laws, 2025. URL <https://arxiv.org/abs/2506.05333>.
- Yuzhang Shang, Mu Cai, Bingxin Xu, Yong Jae Lee, and Yan Yan. Llava-prumerge: Adaptive token reduction for efficient large multimodal models, 2024. URL <https://arxiv.org/abs/2403.15388>.
- Charlie Snell, Jaehoon Lee, Kelvin Xu, and Aviral Kumar. Scaling LLM Test-Time Compute Optimally can be More Effective than Scaling Model Parameters, 2024. URL <https://arxiv.org/abs/2408.03314>.
- Mingjie Sun, Xinlei Chen, J. Zico Kolter, and Zhuang Liu. Massive Activations in Large Language Models. *arXiv preprint arXiv:2402.17762*, 2024.

-
- Xiaoyu Tian, Junru Gu, Bailin Li, Yicheng Liu, Yang Wang, Zhiyong Zhao, Kun Zhan, Peng Jia, Xianpeng Lang, and Hang Zhao. DriveVLM: The Convergence of Autonomous Driving and Large Vision-Language Models, 2024. URL <https://arxiv.org/abs/2402.12289>.
- Philippe Tillet, Hsiang-Tsung Kung, and David Cox. Triton: An intermediate language and compiler for tiled neural network computations. In *Proceedings of the 2nd ACM SIGPLAN International Workshop on Machine Learning and Programming Languages*, 2019.
- Ashish Vaswani, Noam Shazeer, Niki Parmar, Jakob Uszkoreit, Llion Jones, Aidan N. Gomez, Lukasz Kaiser, and Illia Polosukhin. Attention is all you need, 2023. URL <https://arxiv.org/abs/1706.03762>.
- Jesse Vig and Yonatan Belinkov. Analyzing the Structure of Attention in a Transformer Language Model, 2019. URL <https://arxiv.org/abs/1906.04284>.
- Zhongwei Wan, Ziang Wu, Che Liu, Jinfang Huang, Zhihong Zhu, Peng Jin, Longyue Wang, and Li Yuan. LOOK-M: Look-Once Optimization in KV Cache for Efficient Multimodal Long-Context Inference, 2024. URL <https://arxiv.org/abs/2406.18139>.
- Fei Wang, Xingyu Fu, James Y. Huang, Zekun Li, Qin Liu, Xiaogeng Liu, Mingyu Derek Ma, Nan Xu, Wenxuan Zhou, Kai Zhang, Tianyi Lorena Yan, Wenjie Jacky Mo, Hsiang-Hui Liu, Pan Lu, Chunyuan Li, Chaowei Xiao, Kai-Wei Chang, Dan Roth, Sheng Zhang, Hoifung Poon, and Muhao Chen. MuirBench: A Comprehensive Benchmark for Robust Multi-image Understanding, 2024a. URL <https://arxiv.org/abs/2406.09411>.
- Peng Wang, Shuai Bai, Sinan Tan, Shijie Wang, Zhihao Fan, Jinze Bai, Keqin Chen, Xuejing Liu, Jialin Wang, Wenbin Ge, Yang Fan, Kai Dang, Mengfei Du, Xuancheng Ren, Rui Men, Dayiheng Liu, Chang Zhou, Jingren Zhou, and Junyang Lin. Qwen2-VL: Enhancing Vision-Language Model’s Perception of the World at Any Resolution, 2024b. URL <https://arxiv.org/abs/2409.12191>.
- Ziao Wang, Yuhang Li, Junda Wu, Jaehyeon Soon, and Xiaofeng Zhang. FinVis-GPT: A Multimodal Large Language Model for Financial Chart Analysis, 2023. URL <https://arxiv.org/abs/2308.01430>.
- Zichen Wen, Yifeng Gao, Shaobo Wang, Junyuan Zhang, Qintong Zhang, Weijia Li, Conghui He, and Linfeng Zhang. Stop looking for important tokens in multimodal language models: Duplication matters more, 2025. URL <https://arxiv.org/abs/2502.11494>.
- Thomas Wolf, Lysandre Debut, Victor Sanh, Julien Chaumond, Clement Delangue, Anthony Moi, Pierric Cistac, Tim Rault, Rémi Louf, Morgan Funtowicz, Joe Davison, Sam Shleifer, Patrick von Platen, Clara Ma, Yacine Jernite, Julien Plu, Canwen Xu, Teven Le Scao, Sylvain Gugger, Mariama Drame, Quentin Lhoest, and Alexander M. Rush. HuggingFace’s Transformers: State-of-the-art Natural Language Processing, 2020. URL <https://arxiv.org/abs/1910.03771>.
- Peng Xia, Siwei Han, Shi Qiu, Yiyang Zhou, Zhaoyang Wang, Wenhao Zheng, Zhaorun Chen, Chenhang Cui, Mingyu Ding, Linjie Li, et al. Mmie: Massive multimodal interleaved comprehension benchmark for large vision-language models. *arXiv preprint arXiv:2410.10139*, 2024.
- Guangxuan Xiao, Jiaming Tang, Jingwei Zuo, Junxian Guo, Shang Yang, Haotian Tang, Yao Fu, and Song Han. DuoAttention: Efficient Long-Context LLM Inference with Retrieval and Streaming Heads, 2024a. URL <https://arxiv.org/abs/2410.10819>.
- Guangxuan Xiao, Yuandong Tian, Beidi Chen, Song Han, and Mike Lewis. Efficient Streaming Language Models with Attention Sinks, 2024b. URL <https://arxiv.org/abs/2309.17453>.
- Mingyu Yang, Mehdi Rezagholizadeh, Guihong Li, Vikram Appia, and Emad Barsoum. Zebra-Llama: Towards Extremely Efficient Hybrid Models, 2025. URL <https://arxiv.org/abs/2505.17272>.

-
- Shunyu Yao, Dian Yu, Jeffrey Zhao, Izhak Shafran, Thomas L. Griffiths, Yuan Cao, and Karthik Narasimhan. Tree of Thoughts: Deliberate Problem Solving with Large Language Models, 2023. URL <https://arxiv.org/abs/2305.10601>.
- Kaining Ying, Fanqing Meng, Jin Wang, Zhiqian Li, Han Lin, Yue Yang, Hao Zhang, Wenbo Zhang, Yuqi Lin, Shuo Liu, et al. Mmt-bench: A comprehensive multimodal benchmark for evaluating large vision-language models towards multitask agi. *arXiv preprint arXiv:2404.16006*, 2024.
- Jingyang Yuan, Huazuo Gao, Damai Dai, Junyu Luo, Liang Zhao, Zhengyan Zhang, Zhenda Xie, Y. X. Wei, Lean Wang, Zhiping Xiao, Yuqing Wang, Chong Ruan, Ming Zhang, Wenfeng Liang, and Wangding Zeng. Native Sparse Attention: Hardware-Aligned and Natively Trainable Sparse Attention, 2025. URL <https://arxiv.org/abs/2502.11089>.
- Manzil Zaheer, Guru Guruganesh, Avinava Dubey, Joshua Ainslie, Chris Alberti, Santiago Ontanon, Philip Pham, Anirudh Ravula, Qifan Wang, Li Yang, and Amr Ahmed. Big Bird: Transformers for Longer Sequences, 2021. URL <https://arxiv.org/abs/2007.14062>.
- Zhenyu Zhang, Ying Sheng, Tianyi Zhou, Tianlong Chen, Lianmin Zheng, Ruisi Cai, Zhao Song, Yuandong Tian, Christopher Ré, Clark Barrett, Zhangyang Wang, and Beidi Chen. H₂O: Heavy-Hitter Oracle for Efficient Generative Inference of Large Language Models, 2023. URL <https://arxiv.org/abs/2306.14048>.
- Bingchen Zhao, Yongshuo Zong, Letian Zhang, and Timothy Hospedales. Benchmarking multi-image understanding in vision and language models: Perception, knowledge, reasoning, and multi-hop reasoning. *arXiv preprint arXiv:2406.12742*, 2024.

A ATTENTION SPARSITY PATTERNS FOR ADDITIONAL MODELS

While we evaluated the performance of BlindSight on Qwen2-VL, Qwen2.5-VL and Gemma in this paper; we expect that BlindSight can be applied to other VLMs as well. As shown in Fig. 6, we observe the presence of sparse attention layers in VLMs such as Qwen3-VL and Llama 4.

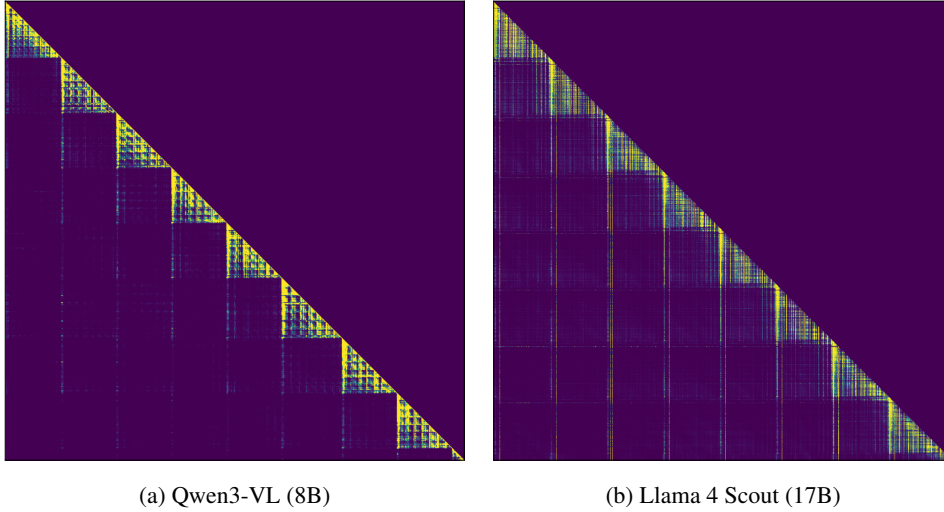


Figure 6: Sparse attention matrices observed in other VLMs

B SPARSITY ANALYSIS

We analyze the distribution of the head-types selected across a dataset using the prompt-level characterization scheme discussed in Algorithm 1. As observed in Fig. 7, a single mask category tends to dominate within a layer across multiple prompts. However, there tends to be a non-negligible fraction selecting other sparsity masks.

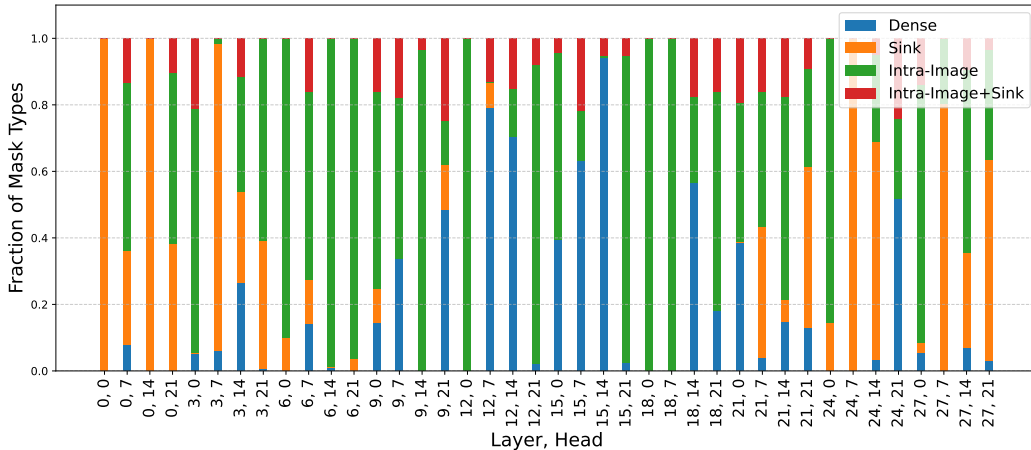


Figure 7: Distribution of sparse mask categories shown for select attention heads across the MMIU dataset using the prompt-level characterization scheme for Qwen 2.5-VL (7B).

C ATTENTION SINK POSITIONS IN GEMMA 3

Fig. 8 represents the attention matrices for different attention heads in the Gemma 3 (4B) model. As shown in the figure, inter-image attention occurs mainly through attention sinks. However, these attention sinks are located at fixed offsets within the image as opposed to the image boundary in the case of Qwen models.

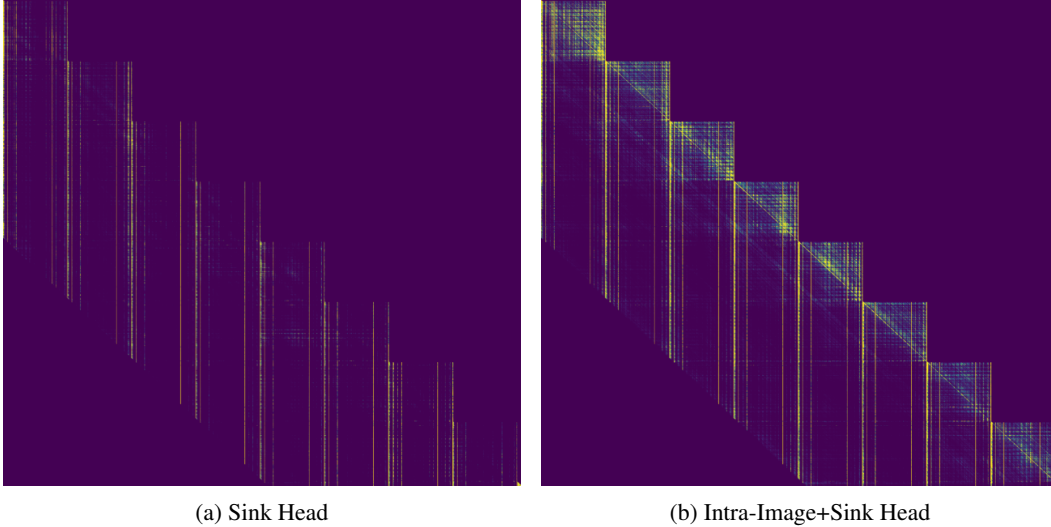


Figure 8: Attention sink positions in Gemma 3

D ABLATION STUDIES FOR HYPERPARAMETERS

Configuring α_{layer} , γ_d and γ_s is essential for the optimal configuration of BlindSight. We ensure that the hyperparameters (apart from the one being varied) remain fixed to their default values of $\alpha_{layer} = 0.1$, $\gamma_d = 0.25$ and $\gamma_s = 0.6$.

D.1 IMPACT OF α_{layer} FOR PROMPT-LEVEL CHARACTERIZATION

α_{layer} sets the NMSE threshold above which the default dense pattern is selected for that particular prompt. A lower value of α_{layer} increases the occurrence of dense heads.

D.1.1 IMPACT OF FIXED α_{layer} FOR QWEN

Across the Qwen models, we fix α_{layer} across layers. A higher α_{layer} leads to a higher model sparsification (Fig. 9). Consequently, performance declines as the fraction of dense masks in the sparsified model is reduced.

α_{layer}	0.05	0.1	0.2	0.4
MuirBench Accuracy (%)	61.71	61.64	56.62	51.49

Table 3: Impact of selecting α_{layer} in Qwen2.5-VL (32B)

D.1.2 IMPACT OF LINEAR α_{layer} FOR GEMMA 3

Fig. 10a represents the attention head type distribution in the Gemma 3 model using a fixed α_{layer} . In this setting, we observe that the initial layers have a higher number of sparse heads. Prior works Cai et al. (2025) have shown that the initial layers are more sensitive to sparsification. Based on this, we employ a linearly increasing threshold α_{layer} to limit sparsification in the initial layers,

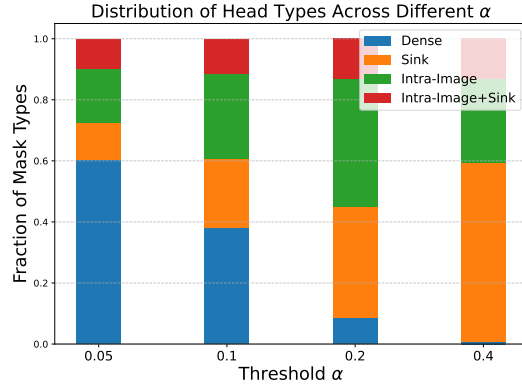
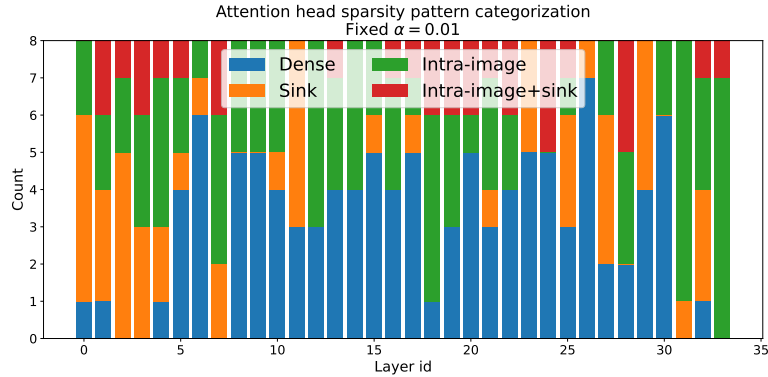
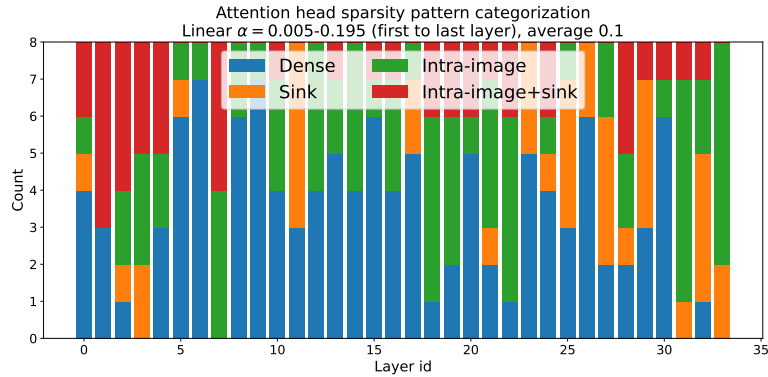


Figure 9: Attention head distribution in Qwen2.5-VL (32B) with different fixed α_{layer}

i.e $\alpha_{layer} = 0.005 + (0.195 - 0.005) * \frac{layer_{idx}}{num_{layers}}$ for Gemma 3 (12B). When handling a smaller model with lower sparsity such as Gemma 3 (4B), we recommend reducing the thresholds to preserve performance, i.e $\alpha_{layer} = 0.001 + (0.099 - 0.001) * \frac{layer_{idx}}{num_{layers}}$. Fig. 10b represents the attention head distribution for linear α_{layer} . This schedule promotes the selection of dense heads in the initial layers. We find that this strategy improves the end-to-end accuracy of the Gemma 3 models for several benchmarks (Table 4). Note that for the Qwen models, the accuracy does not change between the linear and fixed schemes.



(a) Fixed α_{layer} (0.1)



(b) Linear α_{layer} (0.005 to 0.195)

Figure 10: Attention head distribution for Gemma 3 (4B) with different α_{layer} strategies

Gemma 3 (4B)					
	MMIU	MANTIS	MUIRBench	MIRB	MMT
Linear α_{layer}	35.01	60.19	33.93	51.34	54.76
Fixed α_{layer}	34.78	58.99	33.58	46.50	54.37

Gemma 3 (12B)					
	MMIU	MANTIS	MUIRBench	MIRB	MMT
Linear α_{layer}	33.95	68.25	46.78	53.76	59.83
Fixed α_{layer}	33.83	68.20	45.81	49.74	58.55

Table 4: Accuracy (%) for fixed and linear α_{layer} in Gemma 3 models

D.2 IMPACT OF γ_d AND γ_s FOR DATASET-LEVEL AGGREGATION

γ_d and γ_s are used in the Dataset-Level Aggregation step to merge individual sparsity mappings for different prompts. γ_d is a threshold on the fraction of dense heads across prompts, used to qualify a given head as a dense head. A higher value of γ_d leads to a configuration with a lower proportion of dense heads (Fig. 11a). α_{layer} and γ_d control the presence of dense heads in the model.

γ_d	0.1	0.25	0.4
MuirBench Accuracy (%)	61.64	61.64	58.62

Table 5: Impact of varying γ_d in Qwen2.5-VL (32B)

γ_s serves to control the distribution of masks selected among the different sparse masks. Intra-Image+Sink masks are a superset of intra-image and sink masks. Replacing Sink and Intra-Image heads with Intra-Image+Sink heads (Fig. 11b) is not expected to affect the accuracy.

γ_s	0.4	0.6	0.8
MuirBench Accuracy (%)	61.64	61.64	61.79

Table 6: Impact of varying γ_s in Qwen2.5-VL (32B)

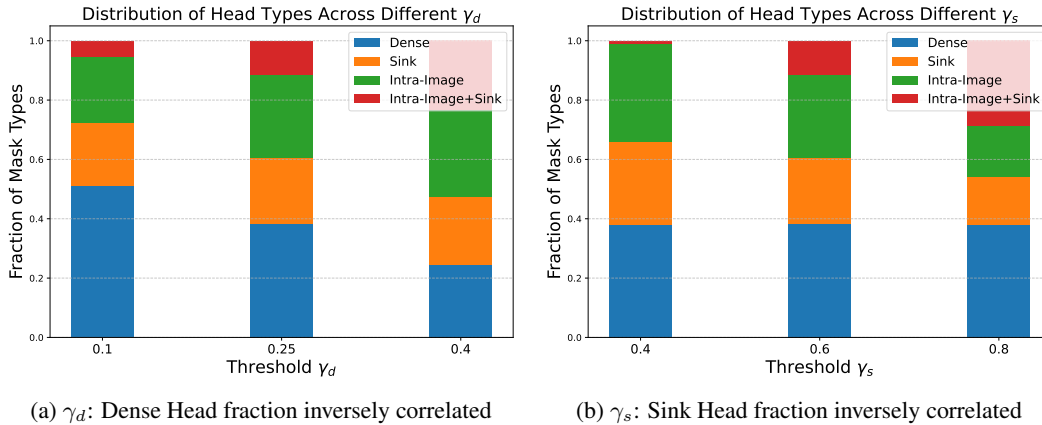


Figure 11: Head distribution with varying γ_d and γ_s in Qwen2.5-VL (32B)

D.3 ACCURACY-FLOPS TRADE-OFFS

BlindSight’s hyperparameters control the distribution of the layer categories in the sparsified model. Increased sparsity is expected to result in lower TTFT, but at the cost of accuracy. This behavior can be observed studying the FLOPS savings across different α_{layer} (Appendix D.1.1). In Fig. 12, we compare the attention FLOPs savings on MuirBench Wang et al. (2024a) for different sparsity levels. Note that variations in the prompt structure (number of images, image dimensions) lead to a distribution in FLOPs savings per α_{layer} . Below a certain sparsification level ($\alpha_{layer} \leq 0.1$), the performance of the sparse model saturates. We suggest that users conduct experimental studies on their end use-case to identify this knee point.

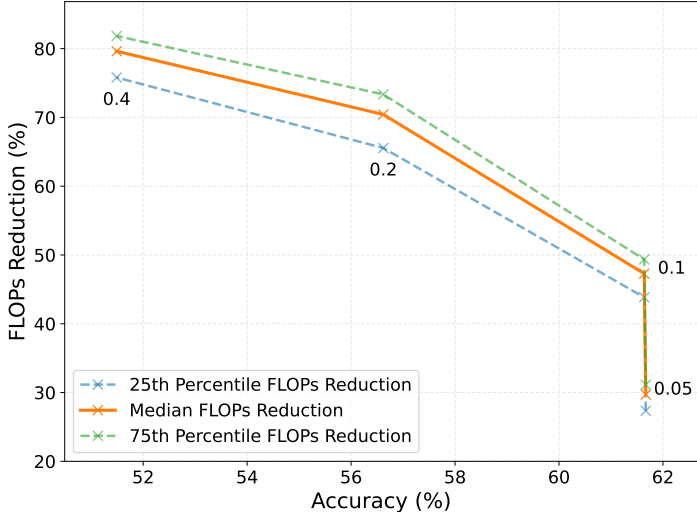


Figure 12: Distribution of attention FLOPs saved on the Qwen 2.5-VL (32B) on the MuirBench evaluation for varying α_{layer} (annotated).

E DETAILS ON MULTI-IMAGE COMPREHENSION BENCHMARKS

MMIU Meng et al. (2024): Evaluates VLMs on multi-image prompts across multiple tasks encompassing 7 types of relationships such as semantic content, temporal relations and spatial understanding. This includes high-level tasks such as captioning, image ordering, similarity detection and text-to-image retrieval.

MuirBench Wang et al. (2024a): Provides robust assessment through 12 diverse multi-image tasks spanning 10 categories of relations (2,600 multiple-choice questions with 11,264 images) such as scene understanding, visual retrieval, geographic understanding, diagram understanding and ordering. This benchmark also includes unanswerable variants.

MANTIS Jiang et al. (2024a): Evaluates multi-image model capabilities through a hand-curated dataset consisting of challenging image understanding questions comparing two images.

MIRB Zhao et al. (2024): Benchmarks multi-image understanding across four evaluation dimensions: perception tasks (image jigsaw, counting, attribute matching), visual world knowledge (sight-seeing locations, food comparisons), reasoning (code understanding, visual analogy, 3D scene understanding), and multi-hop reasoning (synthetic logic chains).

MMT-Bench Ying et al. (2024): Assesses VLMs on 32 core competencies and 162 sub-tasks involving multi-image comprehension. This includes scenarios involving perception, summarization, ordering, retrieval, reasoning, visual coding and OCR detection.

MMIE Xia et al. (2024): Evaluates VLMs on interleaved multimodal comprehension tasks across 20K curated queries spanning 12 fields and 102 sub-fields including mathematics, coding, physics, literature, health and arts.

F BLINDSIGHT SAMPLE OUTPUT

The evaluated benchmarks cover both multiple choice and reasoning-based questions. The LLM was observed to reason in both cases, confirming that BlindSight does not affect the decode phase. We highlight sample responses of a model using BlindSight below.

Example 1: Train Scheduling

Question: The image below shows the current time <image1>. And the image below shows the departure times for all trains departing today <image2>. Find the destination city for the next scheduled train. Follow the steps to answer the question. You should provide a detailed reasoning process and justification for your answer.

Ground Truth Answer: Philadelphia

BlindSight Answer:

###Problem Breakdown:\nWe need to determine the destination city for the next scheduled train based on the current time and the list of train departure times.\n\n###

Step 1: Determine the Current Time\n- The clock in the first image shows the time as **9:00 AM**.\n\n###

Step 2: Analyze the Train Schedule\n\nThe train schedule is provided in the second image, which lists the departure times, destination cities, and train names. Here is the schedule:\n\n| Departure Time | Destination City | Train Name |\n|-----|-----|-----|\n| 04:02 | Los Angeles | Alpha Train |\n| 06:28 | Miami | Gamma Train |\n| 06:39 | San Jose | Max Train |\n| 09:24 | Philadelphia | Fast Train |\n| 09:53 | Winsor | Omega Train |\n\n

Step 3: Identify the Next Scheduled Train\n- The current time is **9:00 AM**.\n- We need to find the next train that departs after **9:00 AM**.\n\n###

Comparison with Each Train:\n\n1. **Alpha Train (04:02)**: This train has already departed (before 9:00 AM).\n2.

Gamma Train (06:28): This train has already departed (before 9:00 AM).\n3.

Max Train (06:39): This train has already departed (before 9:00 AM).\n4.

Fast Train (09:24): This train departs at **9:24 AM**, which is after the current time of **9:00 AM**.\n5.

Omega Train (09:53): This train departs at **9:53 AM**, which is also after the current time of **9:00 AM**, but it is not the next train since the Fast Train departs earlier.\n\n###

Step 4: Determine the Next Train\n- The next train after **9:00 AM** is the **Fast Train**, which departs at **9:24 AM**.\n\n###

```

**Step 5: Identify the Destination City**\n- The destination city
  for the Fast Train is **Philadelphia**.\n\n###

**Final Answer:**\n\nThe destination city for the next scheduled train
  is **Philadelphia**.\n\n\boxed{Philadelphia}\n"

```

Example 2: Computing Area

Question: William is designing a sports field shaped like the cyan parallelogram in the following image <image1>. They plan to mark the boundary around the perimeter using synthetic turf. The price per unit length is given in the following figure <image2>. What would be the total cost for this material? All the computations are rounded to two places of decimal.\n You should provide a detailed reasoning process and justification for your answer.\n

Ground Truth Answer: 128.00

BlindSight Answer:

```

### **Step 1: Identify the shape and dimensions**
The sports field is shaped like a parallelogram. From the image:
- One pair of opposite sides has a length of 999 units.
- The other pair of opposite sides has a length of 777 units.

### **Step 2: Calculate the perimeter of the parallelogram**
The perimeter PPP of a parallelogram is given by the formula:


$$P=2X(\text{length of one pair of opposite sides}+\text{length of the other pair of opposite sides})$$


Substituting the given values:

$$P=2X(9+7)=2X16 = 32$$

So, the perimeter of the parallelogram is 32 units.

### **Step 3: Determine the price of synthetic turf per unit length**
**
From the table provided in the second image, the price of synthetic turf is 4currency units per unit length.

### **Step 4: Calculate the total cost**
The total cost CCC is the product of the perimeter and the price per unit length:

$$C=\text{Perimeter}X\text{Price per unit length}$$

Substituting the values:

$$C=32X4=128$$


### **Final Answer:**
The total cost for marking the boundary with synthetic turf is:
128

```

G FLOPS REDUCTION FOR EVALUATED BENCHMARKS

BlindSight results in savings in the attention FLOPs due to increased sparsity. We summarize the FLOPs reduction in the attention computation for all the evaluated benchmarks in Table 7. We evaluate these metrics on the MuirBench Wang et al. (2024a) dataset. The table highlights the statistics (Q_1 : 25th percentile, Q_2 : Median, Q_3 : 75th percentile) of the percentage of FLOPs saved across all attention layers in the model, computed across the various prompt structures in the benchmark. Note that while Qwen models allow for flexible tokenization per image (1280-5120 in our setup), Gemma models fix this to 128 vision tokens/image. With BlindSight masking primarily the inter-image component of the attention, a reduced fraction of FLOPs are saved on the Gemma models.

Qwen2-VL (7B)						
	MMIU	MANTIS	MuirBench	MIRB	MMT	MMIE
Q_1	26.69	28.52	40.72	17.51	35.94	31.01
Q_2 (Median)	39.18	29.16	45.25	41.84	44.00	31.46
Q_3	47.07	37.98	47.98	46.28	46.86	32.96
Qwen2.5-VL (7B)						
	MMIU	MANTIS	MuirBench	MIRB	MMT	MMIE
Q_1	30.79	32.97	44.72	15.47	39.38	35.76
Q_2 (Median)	43.03	33.91	48.80	45.95	47.45	36.28
Q_3	50.29	41.71	51.26	49.91	50.06	38.01
Qwen2.5-VL (32B)						
	MMIU	MANTIS	MuirBench	MIRB	MMT	MMIE
Q_1	31.12	33.47	43.84	19.75	39.52	36.15
Q_2 (Median)	42.19	34.31	47.29	45.04	45.97	36.97
Q_3	48.42	40.96	49.35	48.36	48.20	38.41
Gemma 3 (4B)						
	MMIU	MANTIS	MuirBench	MIRB	MMT	MMIE
Q_1	9.06	11.50	28.76	32.38	19.55	25.71
Q_2 (Median)	23.51	12.19	31.81	35.09	27.09	29.08
Q_3	30.22	17.82	33.20	36.04	28.71	30.64
Gemma 3 (12B)						
	MMIU	MANTIS	MuirBench	MIRB	MMT	MMIE
Q_1	11.91	14.98	37.83	42.59	25.70	25.77
Q_2 (Median)	30.93	15.88	41.84	46.15	35.64	29.08
Q_3	37.83	23.29	43.66	47.40	37.77	30.64

Table 7: Attention FLOPs reduction (%) statistics across evaluated benchmarks

H ROBUSTNESS TO CHARACTERIZATION DATASET

We highlight the robustness of BlindSight to the characterization dataset in this section. Note that our previous experimental evaluations had utilized the MMIU Meng et al. (2024) dataset. In Table 8, we observe that characterization on the MuirBench Wang et al. (2024a) benchmark results in performance similar to the MMIU-based characterization. In general, we recommend the use of a multi-image dataset with diversity in prompt structure.

I ROBUSTNESS TO IMAGE TOKENIZATION LENGTH

Qwen-style models utilize a flexible image tokenization scheme. In our Qwen evaluation discussed in Table 1, we configure a range between 1280 and 5120 tokens/image. We now study BlindSight’s performance with a fixed number of tokens per image. We observe that BlindSight’s performance does not significantly degrade on the MuirBench Wang et al. (2024a) evaluation compared to the baseline (Table 9) across token lengths per image.

Benchmark	MMIU	MANTIS	MuirBench
Original	44.67	72.51	61.87
BlindSight (MMIU Char.)	44.10	70.62	61.64
BlindSight (MuirBench Char.)	43.90	70.33	62.06

Table 8: Accuracy (%) on MuirBench for Qwen2.5-VL (32B) w/ diff. char. datasets.

Tokenization Length	320	640	1280	2560	5120
Original	62.14	62.83	62.29	61.13	61.10
BlindSight	61.75	61.79	61.38	60.67	60.53

Table 9: Accuracy (%) on MuirBench for Qwen2.5-VL (32B) w/ diff. image tokenization length

J COMPARISON WITH TOKEN PRUNING AND COMPRESSION TECHNIQUES

Several works have focused on different approaches for optimizing the inference and training runtime in VLMs; including token pruning/merging, model compression (quantization) and sparse attention. In this work, we specifically focus on sparsifying the attention matrix to reduce computation.

Another complementary approach to optimization is through token compression or pruning. Prior works such as Chen et al. (2024a); Alvar et al. (2025); Shang et al. (2024); Wen et al. (2025); Gong et al. (2024) have focused on using attention scores or token similarity to reduce the number of visual tokens by pruning or merging redundant tokens. Furthermore, existing token pruning and merging approaches have focused on single image or video benchmarks. Note that in this work, we specifically focus on multi-image inputs. We have shown previously that the inter-image attention component dominates the overall attention computation as the number of images in the prompt increase (Fig. 1b). The lack of evaluation and algorithm design based on multi-image benchmarks in existing token pruning/merging approaches makes it challenging to perform a meaningful quantitative comparison with BlindSight. We now highlight BlindSight’s advantage against pruning with theoretical estimates and showcase its compatibility with experimental evidence.

Fig. 13 compares the theoretical attention FLOPs of token pruning and BlindSight. Note that the y-axis here is in a logarithmic scale. The attention computation requirement with pruning still remains quadratic. However, BlindSight leverages inter-image and intra-image sparsity in VLMs; resulting in a sub-quadratic complexity.

We believe that token compression and BlindSight’s sparse attention are orthogonal to each other. With this aim, we studied the behavior of DivPrune Alvar et al. (2025), a token pruning approach, on the Qwen2-VL (7B) model. We analyzed the attention matrices with BlindSight and BlindSight + DivPrune (90% pruning) in Fig. 14. We note that the original attention sparsity patterns are retained with token compression. Attention heads that exhibit only intra-image attention (top row) do not attend to other images and are not affected by the token compression performed within an

image. Attention heads that use sinks for inter-image attention (lower row) use similar sinks for compressed tokens as well, demonstrating that the proposed delimiter token based attention sink approach is robust to pruning.

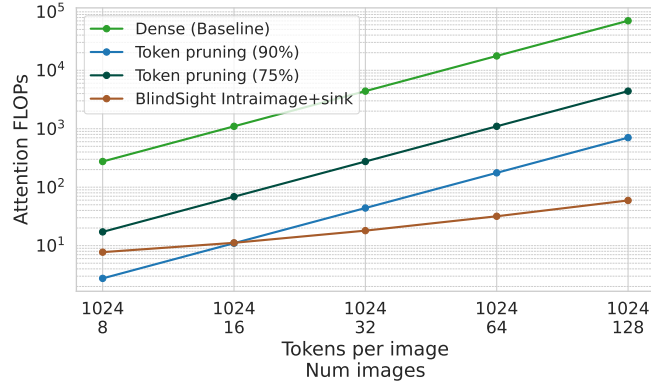


Figure 13: Theoretical attention FLOPs vs context length for BlindSight and token pruning.

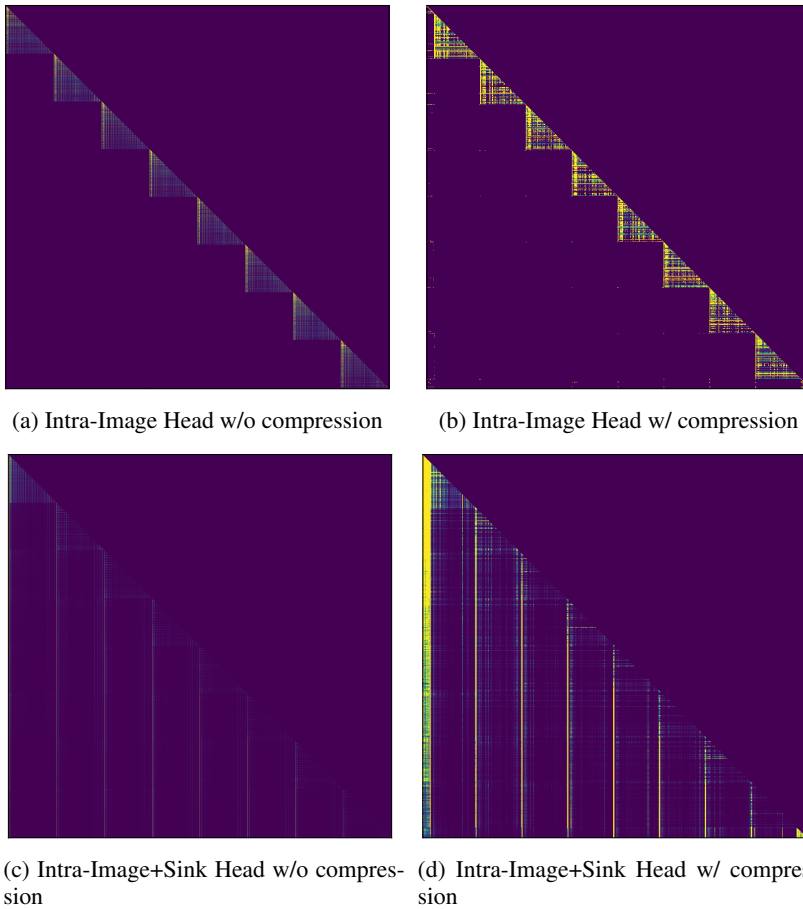


Figure 14: Attention scores w/ and w/o token compression. VLM sparsity patterns persist with 90% token compression.

K BLINDSIGHT FOR VIDEO INPUTS

The Qwen3-VL model Bai et al. (2025a), unlike previous VLMs, introduces delimiter tokens that bound every frame in a video, along with text-based time stamps. This aligns videos to the multi-input image processing scheme leveraged by BlindSight. We observe a lack of inter-image attention as shown in Fig. 15.

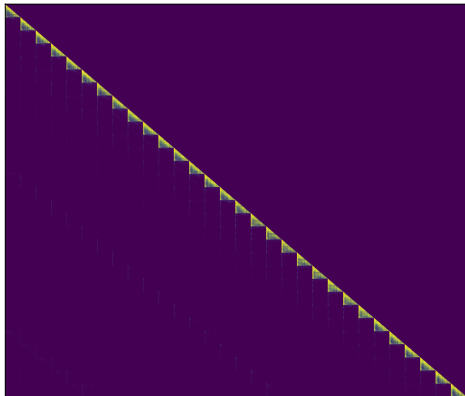


Figure 15: Sparse attention observed in Qwen3-VL (8B) processing videos.

We conduct a preliminary evaluation of BlindSight on video inputs with per-frame delimiters using the Video-MME Fu et al. (2025) benchmark. Video-MME is a comprehensive video analysis benchmark featuring 900 diverse videos (254 hours total) across six visual domains with durations from 11 seconds to 1 hour. Videos are annotated with 2,700 multiple-choice questions. It assesses temporal reasoning, cross-modal understanding and long-context memory. For our preliminary proof-of-concept evaluation, we use the Qwen3-VL-8B-Instruct model. We selected 30 evenly spaced frames from each video without subtitles, with every image tokenized between 128 and 256 tokens. We aim to further study static sink-based sparsity patterns for video inputs in the future.

Benchmark	Video-MME (Short)	Video-MME (Medium)	Video-MME (Long)
Original	72.30	59.00	48.90
BlindSight	70.90	57.90	49.10

Table 10: Accuracy (%) on Video-MME (Short, Medium and Long Videos) for Qwen3-VL (8B)

L BLINDSIGHT ATTENTION KERNEL

BlindSight assigns a sparsity pattern category to each attention head. The corresponding attention mask is constructed online for a given query using the indices of start and end tokens for text and images. To achieve practical speedup on GPUs, a custom compute kernel that leverages the available sparsity to reduce computation and runtime is required. This section describes the implementations and optimizations used in the BlindSight kernel.

L.1 OVERVIEW

The proposed custom kernel is implemented using Triton. Similar to the Flash Attention kernel Dao et al. (2022), the BlindSight kernel divides the attention computation into smaller tiles. For sparse heads, the Triton-based kernel receives additional information alongside queries, keys, and values to avoid computing empty (i.e., completely sparse) tiles. We revert to the Triton-based Flash Attention kernel for dense heads.

The kernel consists of four different subroutines, where a suitable subroutine is selected for a given tile based on the types of query and key tokens (text or image) in the tile. Tiles handling text query tokens must visit all tiles in the key and value matrices and are therefore handled through a Triton-based flash attention subroutine (**dense_attention**). Tiles handling a mix of text and image query tokens will need to visit every tile in the key and value matrices. These may need to mask out inter-image or intra-image attentions depending on the head type. This case will be handled by a subroutine similar to the dense subroutine with additional masking logic to support the various head types. We refer to this as the **masked_attention** subroutine. Finally, tiles that handle only image query tokens can be completely skipped if all keys in a tile are masked out by the selected sparsity pattern. In addition to mask construction, logic is required to determine which tiles have unmasked keys that need to be processed. These are handled through two different subroutines; one to handle the attention sinks (**sink_attention**) and one to handle intra-image attention (**intra_image_attention**). We now discuss the subroutines and summarize optimizations.

L.2 NOTATION

Symbol	Space	Description
B, L	\mathbb{N}	Batch Size, Sequence Length
H, D	\mathbb{N}	Number of heads, Head dimension
Q, K, V	$\mathbb{R}^{L \times D}$	Query, key, and value matrices for a given batch and attention head*.
m, n	\mathbb{N}	Index along the query and key/value sequence lengths
$\text{block}_m, \text{block}_n$	\mathbb{N}	Tile size along the query and key/value sequence lengths.
M	\mathbb{N}	Total tiles in query sequence direction. $M = \lceil \frac{L}{\text{block}_m} \rceil$
N	\mathbb{N}	Total tiles in key-value sequence direction. $N = \lceil \frac{L}{\text{block}_n} \rceil$
q	$\mathcal{R}^{\text{block}_m \times D}$	Tile’s query matrix in shared memory.
k, v	$\mathcal{R}^{\text{block}_n \times D}$	Tile’s key and value matrices in shared memory.

* $Q, K, \text{ and } V$ matrices are for a specific batch and head for brevity.

To construct the masks, the kernel requires extra information about each token. We first define an array $\text{imgid} \in \mathbb{N}^L$ for which an element is assigned a 0 if it is a text token, or an integer identifier of the image to which it belongs. From imgid , we can create a mask of text tokens $\text{istext} \in \mathbb{B}^L$ (True for all text positions) and a mask of image sinks $\text{isingsink} \in \mathbb{B}^L$ (True for all sink positions). **sink_attention** and **intra_image_attention** require pointers to the location of the tiles with valid tokens (i.e., not completely sparse). $\text{sink}_{\text{start}} \in \mathbb{Z}$ points to the start of the image sinks and $\text{sink}_{\text{end}} \in \mathbb{Z}^M$ points to the end of the image sinks under the causal mask for each query tile. $\text{first}_{\text{image}} \in \mathbb{Z}^M$ points to the first location of the intra-image attention in a tile.

L.3 KERNEL IMPLEMENTATION

Algorithm 3 provides a top-level structure of the kernel and subroutine selection process. Fig. 16 represents an example attention matrix, with the horizontal red lines representing the division of the

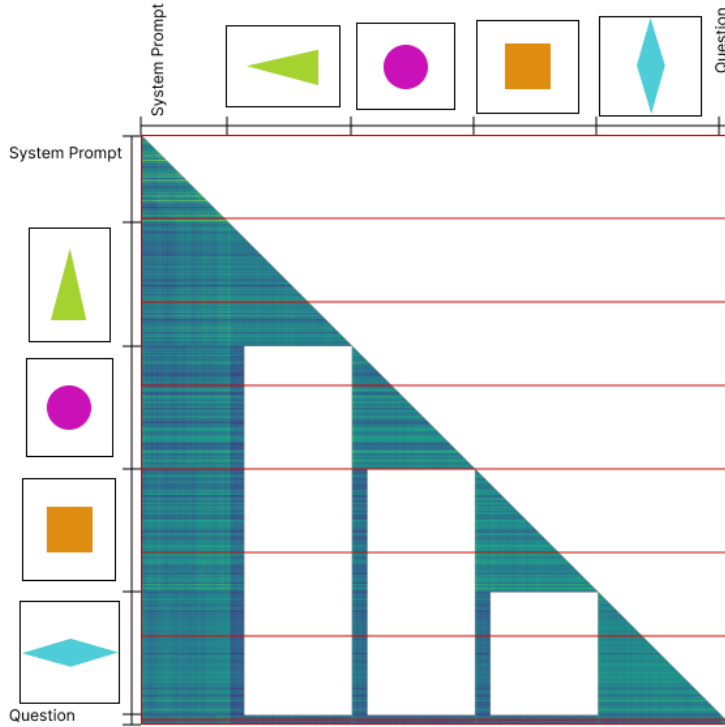


Figure 16: Intra-Image+Sink Head’s attention matrix. Each red box outlines a row consisting all tiles for a subset of query tokens.

attention computation along the query dimension (m). The kernel is parallelized along the batch, head, and query block dimensions, and $(B \times H \times \lceil \frac{L}{\text{block}_m} \rceil)$ workgroups/threadblocks are launched.

L.3.1 DENSE ATTENTION SUBROUTINE

Algorithm 4 describes the subroutine applied to a row consisting of all text queries. In BlindSight, text queries follow the dense mask (with causal or sliding window as per the original model). The dense attention subroutine is applied to the first row in Fig. 16.

L.3.2 MASKED ATTENTION SUBROUTINE

Algorithm 5 describes the attention subroutine applied to all tiles in a row consisting of image and text tokens. In Fig. 16, the masked attention subroutine the last row.

L.3.3 ATTENTION SINK SUBROUTINE

Algorithm 6 describes the subroutine applied to tiles that contain image-only queries and attention sinks. In BlindSight, an attention sink can appear due to text keys and inter-image attention sinks (highlighted by gold and indigo regions in Fig. 17). A naïve approach would result in tiles that make poor use of sparsity considering that the image sinks are interspersed throughout the attention matrix (Fig. 18a).

To further optimize such a scenario, we propose reordering key and value matrices along the N dimension so that attention sinks are grouped together (Fig. 18b). As the kernel traverses the sequence of key/value tokens, the full tiles efficiently utilize the memory bandwidth and the GPU matrix-multiply units. To perform the permutation, we define the permutation vector $N^p \in \mathbb{N}^L$ as $\text{concat}(\{i : \text{istext}_i = \text{True}\}, \{j : \text{isimsink}_j = \text{True}\}, \{k : \neg \text{istext}_k \wedge \neg \text{isimsink}_k\})$.

Algorithm 3 BlindSight Kernel

Input:
 Q, K, V (Query, key and value matrices)
 K^p, V^p (Permuted key and value matrices)
imgid (imgid vector)
istext (istext mask)
isingsink (isingsink mask)
 m (Start of the tile along the query sequence dimension L)
headtype (Mask type in use [dense,image,image_sink,sink])
sink_{start} (The location of the first sink token in the key and value matrices.)
sink_{end} (Array of locations of the last sink in a query tile.)
first_image (Array of locations of the first image in a query tile.)
block _{m} (Size of the tile along the query matrix)
block _{n} (Size of the tile along the key and value matrices)

Output Out (Attention output of tiles for a set of queries in a given attention head)

$q \leftarrow Q[m : m + \text{block}_m]$ ($q \in \mathcal{R}^{\text{block}_m \times D}$)
istext _{m} \leftarrow istext[$m : m + \text{block}_m$] (istext _{m} $\in \mathbb{B}^{\text{block}_m}$)
if all(istext _{m}) **then**
 Out \leftarrow dense_attention($q, K, V, m, \text{block}_m, \text{block}_n$) Alg. 4
else if any(istext _{m}) **then**
 mask _{kv} \leftarrow (istext) if headtype = “image” otherwise (istext | isingsink)
 Out \leftarrow masked_attention($q, K, V, m, \text{istext}_m, \text{mask}_{kv}, \text{block}_m, \text{block}_n$) Alg. 5
else
 mask _{kv} \leftarrow (istext) if headtype = “image” otherwise (istext | isingsink)
 sink_{end} \leftarrow sink_end[m]
 Out \leftarrow sink_attention($q, K^p, V^p, m, \text{mask}_{kv}, \text{sink}_{start}, \text{sink}_{end}, \text{block}_m, \text{block}_n$) Alg. 6
 if headtype = “image” or headtype = “image_sink” **then**
 Out \leftarrow intra_image_attention(Out, $q, K, V, \text{imgid}, \text{first_image}, \text{block}_m, \text{block}_n$) Alg. 7
 end if
end if
return Out

L.3.4 INTRA-IMAGE ATTENTION SUBROUTINE

This subroutine is applied to tiles with only image tokens, i.e. intra-image attention. In Fig. 17, the intra-image attention subroutine is applied to tiles containing green highlighted region. Algorithm 7 represents the approach for this subroutine. Note that since the intra-image attention is concentrated within a region, fewer tiles are required to compute this attention.

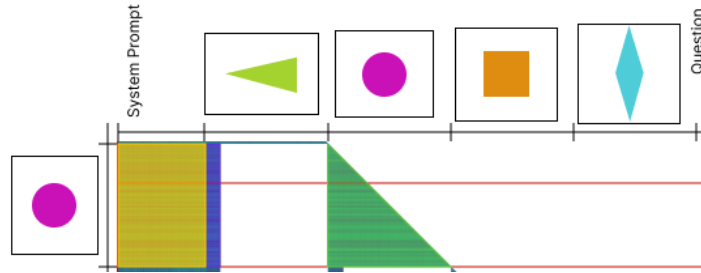
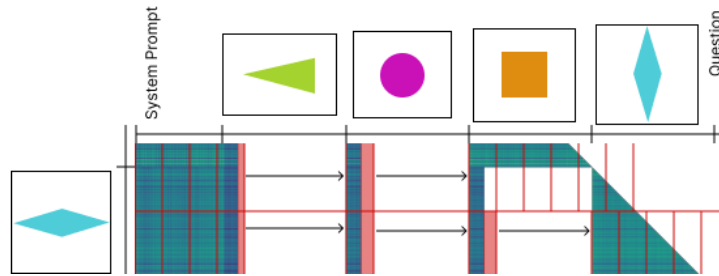
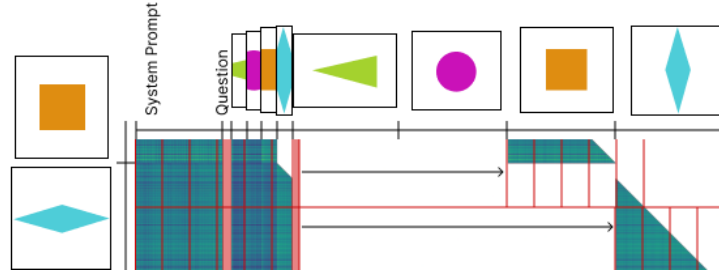


Figure 17: Two rows of the attention matrix shown in Fig. 16 containing only image query tokens. Segments of the attention scores are highlighted in gold, indigo, and green depending on whether they arise from image-text, inter-image, or intra-image attention respectively.



(a) Attention Matrix Before Permutation



(b) Attention Matrix After Permutation. Image sinks have been packed towards the front, saving the kernel from having to calculate an extra tile.

Figure 18: Two rows of the attention matrix shown in Fig. 16 which contain only image query tokens. Red lines outline tiles in both M and N dimensions. Areas highlighted in red show segments which fall within a tile but are numerically masked out, leading to poor GPU utilization.

Algorithm 4 dense_attention

Input:
 $q \in \mathcal{R}^{\text{block}_m \times D}$ (Query tile)
 K, V (Key and value matrices)
 m (Start of the tile along the query sequence dimension)
 block_m (Size of the tile along the query sequence length)
 block_n (Size of the tile along the key/value sequence length)

Output Out

$m_{off} = \{m, m + 1, m + 2, \dots, m + \text{block}_m - 1\}$ ($m_{off} \in \mathbb{N}^{\text{block}_m}$)
 $Out \leftarrow (0)_{\text{block}_m \times D}$ ($Out \in \mathcal{R}^{\text{block}_m \times D}$)
 $l \leftarrow (0)_{\text{block}_m}$ ($l \in \mathcal{R}^{\text{block}_m}$)
 $max \leftarrow (-\infty)_{\text{block}_m}$ ($max \in \mathcal{R}^{\text{block}_m}$)

for n **in** $\text{range}(0, m + \text{block}_m, \text{block}_n)$ **do**
 $k \leftarrow K[n : n + \text{block}_n]$ ($k \in \mathcal{R}^{\text{block}_n \times D}$)
 $v \leftarrow V[n : n + \text{block}_n]$ ($v \in \mathcal{R}^{\text{block}_n \times D}$)
 $s \leftarrow qk^T$
 $n_{off} = \{n, n + 1, n + 2, \dots, n + \text{block}_n - 1\}$ ($n_{off} \in \mathbb{N}^{\text{block}_n}$)
 $s'[i][j] \leftarrow s[i][j]$ if $i \geq j$ else $-\infty$ for $i \in m_{off}$ and $j \in n_{off}$
 $max_n \leftarrow \text{rowmax}(s')$
 $p \leftarrow \exp(s' - max_n)$
 $l_n \leftarrow \text{rowsum}(p)$
 $max^{new} \leftarrow \text{maximum}(max, max_n)$
 $l^{new} \leftarrow \exp(max - max^{new})l + \exp(max_n - max^{new})l_n$
 $Out \leftarrow \exp(max - max^{new})Out + \exp(max_n - max^{new})pv$
 $max \leftarrow max^{new}$
 $l \leftarrow l^{new}$

end for
return Out

Algorithm 5 masked_attention

Input:
 $q \in \mathcal{R}^{\text{block}_m \times D}$ (Query tile)
 K, V (Key and value matrices)
 m (Start of the tile along the query matrices)
 $\text{istext}_m \in \mathbb{B}^{\text{block}_m}$ (Query mask)
 mask_{kv} (Key, value matrix mask)
 block_m (Size of the tile along M dimension)
 block_n (Size of the tile along N dimension)

Output *Out*

$m_{off} = \{m, m + 1, m + 2, \dots, m + \text{block}_m - 1\}$ ($m_{off} \in \mathbb{N}^{\text{block}_m}$)
 $Out \leftarrow (0)_{\text{block}_m \times D}$ ($Out \in \mathcal{R}^{\text{block}_m \times D}$)
 $l \leftarrow (0)_{\text{block}_m}$ ($l \in \mathcal{R}^{\text{block}_m}$)
 $max \leftarrow (-\infty)_{\text{block}_m}$ ($max \in \mathcal{R}^{\text{block}_m}$)
for n in range($0, m + \text{block}_m, \text{block}_n$) **do**
 $k \leftarrow K[n : n + \text{block}_n]$ ($k \in \mathcal{R}^{\text{block}_n \times D}$)
 $v \leftarrow V[n : n + \text{block}_n]$ ($v \in \mathcal{R}^{\text{block}_n \times D}$)
 $s \leftarrow qk^T$
 $\text{mask}_n \leftarrow \text{mask}_{kv}[n : n + \text{block}_n]$ ($\text{mask}_n \in \mathbb{B}^{\text{block}_n}$)
 $\text{mask} \leftarrow \text{istext}_m[:, \text{None}] \text{mask}_n[\text{None}, :]$ ($\text{mask} \in \mathbb{B}^{\text{block}_m \times \text{block}_n}$)
 $n_{off} = \{n, n + 1, n + 2, \dots, n + \text{block}_n - 1\}$ ($n_{off} \in \mathbb{N}^{\text{block}_n}$)
 $\text{mask}_{causal}[i][j] \leftarrow 1$ if $i \geq j$ else 0 for $i \in m_{off}$ and $j \in n_{off}$
 $s' \leftarrow s$ where $\text{mask} \ \& \ \text{mask}_{causal}$ otherwise $-\infty$
 $max_n \leftarrow \text{rowmax}(s')$
 $p \leftarrow \exp(s' - max_n)$
 $l_n \leftarrow \text{rowsum}(p)$
 $max^{new} \leftarrow \text{maximum}(max, max_n)$
 $l^{new} \leftarrow \exp(max - max^{new})l + \exp(max_n - max^{new})l_n$
 $Out \leftarrow \exp(max - max^{new})Out + \exp(max_n - max^{new})pv$
 $max \leftarrow max^{new}$
 $l \leftarrow l^{new}$
end for
return *Out*

Algorithm 6 sink_attention

Input:
 $q \in \mathcal{R}^{\text{block}_m \times D}$ (Query tile)
 K, V (Key and value matrices)
 N^p (Original index of each token)
 m (Start of the tile along the query matrices)
 mask_{kv} (Key, value token mask)
 sink_{start} (Start of each sink)
 sink_{end} (End of each sink)
 block_m (Size of the tile along M dimension)
 block_n (Size of the tile along N dimension)

Output Out

$m_{off} = \{m, m + 1, m + 2, \dots, m + \text{block}_m - 1\}$ ($m_{off} \in \mathbb{N}^{\text{block}_m}$)
 $Out \leftarrow (0)_{\text{block}_m \times D}$ ($Out \in \mathcal{R}^{\text{block}_m \times D}$)
 $l \leftarrow (0)_{\text{block}_m}$ ($l \in \mathcal{R}^{\text{block}_m}$)
 $max \leftarrow (-\infty)_{\text{block}_m}$ ($max \in \mathcal{R}^{\text{block}_m}$)
for n **in range**($\text{sink}_{start}, \text{sink}_{end}, \text{block}_n$) **do**
 $n^p \leftarrow N^p[n : n + \text{block}_n]$ ($n \in \mathbb{N}^{\text{block}_n}$)
 $k \leftarrow K^p[n : n + \text{block}_n]$ ($k \in \mathcal{R}^{\text{block}_n \times D}$)
 $v \leftarrow V^p[n : n + \text{block}_n]$ ($v \in \mathcal{R}^{\text{block}_n \times D}$)
 $s \leftarrow qk^T$
 $\text{mask}_n \leftarrow \text{mask}_{kv}[n^p]$ ($\text{mask}_n \in \mathbb{B}^{\text{block}_n}$)
 $n_{off} = \{n, n + 1, n + 2, \dots, n + \text{block}_n - 1\}$ ($n_{off} \in \mathbb{N}^{\text{block}_n}$)
 $\text{mask}_{causal}[i][j] \leftarrow 1$ if $i \geq j$ else 0 for $i \in m_{off}$ and $j \in n_{off}$
 $s' \leftarrow s$ where $\text{mask}_{causal} \& \text{mask}_n[None, :]$ otherwise $-\infty$
 $max_n \leftarrow \text{rowmax}(s')$
 $p \leftarrow \exp(s' - max_n)$
 $l_n \leftarrow \text{rowsum}(p)$
 $max^{new} \leftarrow \text{maximum}(max, max_n)$
 $l^{new} \leftarrow \exp(max - max^{new})l + \exp(max_n - max^{new})l_n$
 $Out \leftarrow \exp(max - max^{new})Out + \exp(max_n - max^{new})pv$
 $max \leftarrow max^{new}$
 $l \leftarrow l^{new}$
end for
return Out

Algorithm 7 intrainage_attention

Input:

$Out \in \mathcal{R}^{\text{block}_m \times D}$ (Previous Out value for this subroutine to accumulate)
 $q \in \mathcal{R}^{\text{block}_m \times D}$ (Query tile)
 K, V (Key and value matrices)
 m (Start of the tile along the query matrix)
 imgid (The image id vector)
 first_image (Location of the first image)
 block_m (Size of the tile along M dimension)
 block_n (Size of the tile along N dimension)

Output Out

$m_{off} = \{m, m + 1, m + 2, \dots, m + \text{block}_m - 1\}$ ($m_{off} \in \mathbb{N}^{\text{block}_m}$)
 $l \leftarrow (0)_{\text{block}_m}$ ($l \in \mathcal{R}^{\text{block}_m}$)
 $max \leftarrow (-\infty)_{\text{block}_m}$ ($max \in \mathcal{R}^{\text{block}_m}$)
 $\text{first}_{image} = \text{first_image}[m \div \text{block}_m]$
 $\text{imgid}_m \leftarrow \text{imgid}[m : m + \text{block}_m]$ ($\text{imgid}_m \in \mathbb{N}^{\text{block}_m}$)
for n **in** $\text{range}(\text{first}_{image}, m + \text{block}_m, \text{block}_n)$ **do**
 $k \leftarrow K[n : n + \text{block}_n]$ ($k \in \mathcal{R}^{\text{block}_n \times D}$)
 $v \leftarrow V[n : n + \text{block}_n]$ ($v \in \mathcal{R}^{\text{block}_n \times D}$)
 $\text{imgid}_n \leftarrow \text{imgid}[n : n + \text{block}_n]$ ($\text{imgid}_n \in \mathbb{N}^{\text{block}_n}$)
 $s \leftarrow qk^T$
 $mask \leftarrow \text{imgid}_m[:, None] = \text{imgid}_n[None, :]$ ($mask \in \mathbb{B}^{\text{block}_m \times \text{block}_n}$)
 $n_{off} = \{n, n + 1, n + 2, \dots, n + \text{block}_n - 1\}$ ($n_{off} \in \mathbb{N}^{\text{block}_n}$)
 $mask_{causal}[i][j] \leftarrow 1$ if $i \geq j$ else 0 for $i \in m_{off}$ and $j \in n_{off}$
 $s' \leftarrow s$ where $mask \ \& \ mask_{causal}$ otherwise $-\infty$
 $max_n \leftarrow \text{rowmax}(s')$
 $p \leftarrow \exp(s' - max_n)$
 $l_n \leftarrow \text{rowsum}(p)$
 $max^{new} \leftarrow \text{maximum}(max, max_n)$
 $l^{new} \leftarrow \exp(max - max^{new})l + \exp(max_n - max^{new})l_n$
 $Out \leftarrow \exp(max - max^{new})Out + \exp(max_n - max^{new})pv$
 $max \leftarrow max^{new}$
 $l \leftarrow l^{new}$
end for
return Out

M REPRODUCIBILITY STATEMENT

The codebase for reproducing results in this paper is available at <https://anonymous.4open.science/r/BlindSight-AFDC>. The approach can be easily extended to the current and future VLMs released on Hugging Face.